IEEE Access
Multidisciplinary | Rapid Review | Open Access Journal

Received 10 December 2022, accepted 23 December 2022, date of publication 29 December 2022,
date of current version 5 January 2023.

Digital Object Identifier 10.1109/ACCESS.2022.3233223

RESEARCH ARTICLE

Theory and Experiment of Spatial Light Modulation and Demodulation With Multi-Plane Diffraction and Applications

BURHAN GULBAHAR[1], (Senior Member, IEEE), AND AHMET EMRECAN OKSUZ[2]
[1]Department of Electrical and Electronics Engineering, Yasar University, 35100 İzmir, Turkey
[2]The Graduate School of Natural and Applied Sciences, Dokuz Eylül University, 35390 İzmir, Turkey

Corresponding author: Burhan Gulbahar (burhan.gulbahar@yasar.edu.tr)

This work was supported by TÜBİTAK (The Scientific and Technological Research Council of Turkey) under Grant 119E584.

ABSTRACT Spatial light modulation enhances capacity of optical communications by modulating spatial amplitude, phase and polarization degrees of freedom with recent success of orbital angular momentum based architectures. There is a hardware challenge to demodulate large symbol families or high order symbols requiring a general design of spatial light demodulation. Multi-plane diffraction (MPD) recently introduced for improving spatial modulation capabilities in free space optical channels promises utilization at the receiver side as a demodulator. In this article, we theoretically model, numerically simulate and experimentally implement spatial light demodulation based on MPD. Numerical simulations and experimental implementations verify capabilities of MPD for increasing inter-symbol distances at the detector front-end. We obtain approximately two times improvement compared with direct detection for basic design including three diffraction planes as a proof-of-concept and improved performance with increasing number of diffraction planes compared with state-of-the-art single-plane diffraction (SPD) based interferometric receivers. Besides that, we perform, for the first time, experimental implementation of MPD based spatial light modulation. In addition, symmetric-key cryptography application of the proposed system is theoretically presented with low decoder complexity while numerical simulations promise high performance security against intruders. MPD based design is practically applicable and promising for diverse optical architectures including both communications and cryptography as a low-cost, low hardware complexity, passive and high performance design.

INDEX TERMS Multi-plane diffraction, spatial modulation, spatial light modulation, spatial light demodulation, optical communications, all-optical encryption, cryptography.

I. INTRODUCTION

Spatial light modulation modulates phase, amplitude and polarization of wave function or wave-front [1], [2], [3]. It enhances capacity of optical communications by allowing to use spatial degrees of freedom in various architectures [1], [4], [5], [6], [7]. Communication systems based on spatial light modulation exploit orbital angular moment (OAM) [6], [8], [9], [10], [11] and polarization [12], [13] degrees of freedom in free space and fiber optical communications. In addition, visible light communications (VLC) systems exploit spatial light modulators to realize spatially variant polarization states [12], [14]. On the other hand, in spatial light modulation based optical communication architectures, detectors include holographic gratings, various interferometer structures, polarizers or additional spatial light modulators with detailed reviews presented in [10] and [15]. Demodulator inverts phase distribution of the transmitted modulation symbol resulting in a hardware based challenge for large number of symbols and high order modulation such as increased complexity for higher mode numbers in OAM receivers [10]. A phase analyzer needs to be utilized to estimate transmitted phase distribution in more general set-ups. Machine learning approaches are also proposed for

The associate editor coordinating the review of this manuscript and approving it for publication was Guido Lombardi.

efficient demodulation capabilities [16]. As a result, high order optical demodulation with low-complexity hardware and diverse applicability for various spatial modulation based systems is an important challenge.

Multi-plane diffraction (MPD) is recently utilized to define quantum spatial modulation in [17] by emphasizing improvement in the symbol family size and spectral efficiency as a method to improve spatial modulation for optical channels [18], [19], [20], [21]. MPD is further extended to radio frequency (RF) channels by showing the promising capabilities of MPD in also RF communications [22]. Furthermore, MPD set-ups with amplitude and phase masks are experimentally realized for defining all-optical machine learning with promising advantages but not for the purpose of optical modulation or demodulation in free space optical communications [23], [24]. There is not any experimental implementation of MPD based spatial light modulation for optical channels for experimental verification of the design. Furthermore, general modeling for modulating both the phase and amplitudes is not considered in [17]. In addition, it is not clear how to demodulate spatial light modulation symbols by exploiting MPD based architectures by maintaining the same hardware simplicity at the receiver side in comparison with challenges in state-of-the-art architectures [10]. Besides that, there are existing architectures to demodulate OAM modulated waves by using single plane diffraction (SPD) apertures by transforming phase information into interferometric intensity differences at the receivers [25], [26], [27], [28]. The major drawback of these architectures is the requirement of $N-1$ interferometers to detect N OAM modes resulting in practical complexity for high order modulations [10], [28]. MPD based general spatial light demodulation design, theory and experiment are not available as an alternative to SPD based architectures.

In this article, we theoretically design and experimentally implement a generalized spatial light demodulation by exploiting both phase and amplitude modulating MPD design which is applicable to diverse communication systems while promising the simplicity with low-cost diffraction slit design and passive diffraction architecture. In addition, we perform, for the first time, experimental implementation of free space optical MPD design proposed in [17], i.e., quantum spatial modulation, with simple rectangular slit masks for the purpose of verifying spatial modulation capabilities in optical channels. MPD provides a low-complexity and passive architecture for realizing modulation compared with more complex and active modulation designs including liquid crystal based or digital micro-mirror designs [1], [2], [3].

We numerically simulate and experimentally implement spatial light demodulation to decode symbols with small inter-symbol distances as a proof-of-concept while improving inter-symbol distance by $\approx$2 times at maximum compared with the case without demodulation for specific set-up parameters including three diffraction planes at the receiver. Furthermore, it is observed that inter-symbol distance increases with increasing number of planes in MPD based demodulation architecture both in numerical simulation and experimental studies. Therefore, proposed MPD based demodulation design promises important improvements compared with state-of-the-art SPD based interferometric architectures utilized to demodulate spatially modulated signals. Spatial demodulation creates complex interference patterns with promising applications for large symbol families. In the proposed experimental validation, smooth intensity patterns of symbols with small inter-symbol distances are transformed into higher frequency intensity patterns with larger inter-symbol distances by using random spatial masks. Therefore, MPD based interferometric design exploits phase difference of symbols to create more distant interference patterns for different symbols. Therefore, we enhance existing methods based on SPD by proposing MPD to increase the demodulation capability similar to increased spatial modulation capability at the transmitter side presented for quantum spatial modulation [25], [26], [27], [28]. In addition, slit masks are realized with low-cost and low-complexity design, for the first time, based on graphite cylinders allowing to realize complex spatial light modulation and demodulation tasks for free space optical communication and cryptographic applications.

After defining MPD based spatial demodulation for optical communications, we design an all-optical hardware based symmetric-key cryptography system, for the first time, by exploiting only passive MPD design, without any software based decoding complexity. There are various all-optical encryption/decryption mechanisms utilizing symmetric or private-key based mechanism by using spectral shuffling [29] and all-optical logic gates [30], [31]. However, MPD based architecture is not exploited. We numerically simulate protection against an intruder utilizing a random mask at the decoder. The intruder cannot practically find private keys among exponentially large number of possible private masks. Furthermore, our numerical analysis with phase-only modulator masks shows that the intruder observes uniformly distributed phase patterns without any clue to reliably decode if there is no access to private keys.

The contributions presented in this article are summarized as follows:

- We design a novel spatial light demodulation method based on MPD introduced previously only for spatial light modulation purposes while achieving a low-cost, low-complexity and passive hardware design. Numerical simulations and experimental results for SPD show improvements of inter-symbol distances by $\approx$2 times at maximum with three diffraction planes compared with the case without spatial light demodulation. In addition, inter-symbol distances increase with increasing number of diffraction planes by improving performance compared with interferometric state-of-the-art SPD receiver design as a proof-of-concept.
- We improve previous theoretical models for MPD consisting of amplitude modulating slit masks by modeling for both amplitude and phase modulation.

- We, for the first time, experimentally implement both spatial light modulation and demodulation based on MPD. As a proof-of-concept, simple rectangular slits are utilized for experiments.
- We propose a novel diffraction plate design to be utilized for spatial light demodulation purposes by using graphite cylinders with a low-cost and simplified design architecture.
- We present theoretical modeling and numerical simulation of a novel all-optical symmetric-key cryptography system by exploiting MPD based spatial light demodulation design.

Experimental challenges include experimental characterization of MPD based complete spatial light modulation and demodulation architectures with solid evidences about the performance including data rates and error rates. Experimental implementations of high order modulation and demodulation set-ups with many consecutive diffraction planes in MPD are left as future works while only proof-of-concept and low-complexity MPD architectures are implemented with the maximum of four diffraction plates.

The remainder of the paper is organized as follows. In Section II, demodulation architecture based on MPD is introduced and theoretically modeled for general phase-amplitude modulation design. In Section III, MPD modeling based on rectangular slits is presented where only the amplitude is modulated with rectangular slits. Performance of demodulation is numerically simulated in Section IV. In Section V, experimental implementations of both spatial light modulation and demodulation based on rectangular slit based diffraction architectures are presented. Application of demodulation for symmetric-key cryptography algorithm including system design, theoretical modeling and numerical simulations is presented in Section VI. Finally, in Section VII, conclusions are presented.

II. SPATIAL LIGHT DEMODULATION WITH MPD BASED PASSIVE DIFFRACTION

The proposed two-dimensional (2D) spatial light modulation and demodulation design is presented in Fig. 1. Assume that spatially modulated optical signal wave-function $\Psi_m(x, y)$ at the transmitter (Tx) 2D surface for sending information by use of M wave functions with $m \in [1, M]$ is defined as follows:

$$\Psi_m(x, y) = A_m(x, y)\, e^{\imath\, \phi_m(x,y)} \tag{1}$$

where $A_m(x, y)$ and $\phi_m(x, y)$ are the modulation amplitude and phase, respectively. After through the free space channel propagation of length L_c, $\Psi_{r,m}(x, y)$ and $\Psi_{d,m}(x, y)$ are the received and detected inputs at the surfaces of the demodulator and photo-detector (PD) array, respectively, for a passive demodulation set-up without changing the spatial mask each time with respect to m. MPD multiplicative mask $D_j(x, y)$ for $j \in [1, N]$ multiplies incoming wave function on jth plane. In other words, $\Psi_{in}(x, y)$ on jth plane is transformed into $\Psi_{in}(x, y) \times D_j(x, y)$. Each plane has $K_D \times K_D$ pixels with each pixel having side length of W_D and inter-planar planar distances of $L_{D,j,j+1}$ between jth and $(j + 1)$th planes. Modulation is based on quantum spatial modulation defined in [17] exploiting MPD structure where each plane has a mask of $M_{j,m}(x, y)$ for $j \in [1, V]$ depending on m and a total of $K_M \times K_M$ pixels on each plane with pixel side-length of W_M where inter-planar distance is $L_{M,j,j+1}$ between jth and $(j + 1)$th planes. $L_{M,01}$ denotes the distance of laser plane with the source wave function $\Psi_0(x, y)$ to the first plane in modulation.

Received intensity distribution before demodulation is denoted with $I_{r,m}(x, y) = |\Psi_{r,m}(x, y)|^2$ for varying symbol index m as shown in Fig. 1. Intensity is detected with $N_P = N_x \times N_y$ pixels at a longitudinal distance of L_d to the Nth plane of the demodulator. The resulting intensity distribution is the demodulator output $I_{d,m}(x, y) = |\Psi_{d,m}(x, y)|^2$ which is the input to the detector, e.g., maximum-likelihood detection, for estimating $\widehat{m}$. Assuming an additive white Gaussian noise (AWGN) model $n[k_x, k_y]$ at the PD corresponding to the pixel position $(x, y) = (k_x,\ k_y) \times T_s$, the detector input is given as follows:

$$y[k_x, k_y] = I_{d,m}[k_x, k_y]\ + n[k_x, k_y] \tag{2}$$

where $k_x \in [1, N_x]$, $k_y \in [1, N_y]$, $T_s \in \mathbb{R}^+$ is the spatial sampling width of PDs and $I_{d,m}[k_x, k_y]$ is the detected number of photons during sampling period and calculated as follows:

$$I_{d,m}[k_x, k_y] = r_e\, P_m \int_{s_{k_x,-}}^{s_{k_x,+}} \int_{s_{k_y,-}}^{s_{k_y,+}} |\Psi_{d,m}(x, y)|^2\, dx\ dy \tag{3}$$

where $s_{k_a,\pm} \equiv (k_a \pm 1/2)\, T_s$ for integer k_a gives the boundaries of the detector along the axis $a = x$ or y, P_m is the number of photons in a single channel use and r_e is PD responsivity. Propagation from the jth plane to $(j+1)th$ plane with longitudinal distance of $L_{D,j,j+1} \gg \lambda$ is calculated as follows:

$$\Psi_{out}(x, y) = \int_{x_0} \int_{y_0} K_j(x, y, x_0, y_0)\, D_j(x_0, y_0) \times \Psi_{in}(x_0, y_0)\, d\ x_0\, d\ y_0 \tag{4}$$

where $\Psi_{in}(x, y)$ and $\Psi_{out}(x, y)$ denote wave functions on input surfaces of jth and $(j + 1)th$ planes, respectively, and free-space propagation kernel $K_j(x, y, x_0, y_0)$ is defined as follows by neglecting distance dependent phase [17]:

$$K_j(x, y, x_0, y_0) = \frac{e^{\imath\, k\left((x-x_0)^2+(y-y_0)^2\right)\,/\,\left(2\,L_{D,j,j+1}\right)}}{\imath\ \lambda\ L_{D,j,j+1}} \tag{5}$$

where $k \equiv 2\,\pi\ /\ \lambda$ is the wave vector and λ is the wavelength of laser source.

Inter-symbol distance between demodulated symbols $I_{d,i}[k_x, k_y]$ and $I_{d,j}[k_x, k_y]$ for ith and jth symbols, respectively, is defined as follows:

$$d_{i,j} \equiv \sqrt{\sum_{k_x=1}^{N_x} \sum_{k_y=1}^{N_y} |I_{d,i}[k_x, k_y]\ -\ I_{d,j}[k_x, k_y]|^2} \tag{6}$$

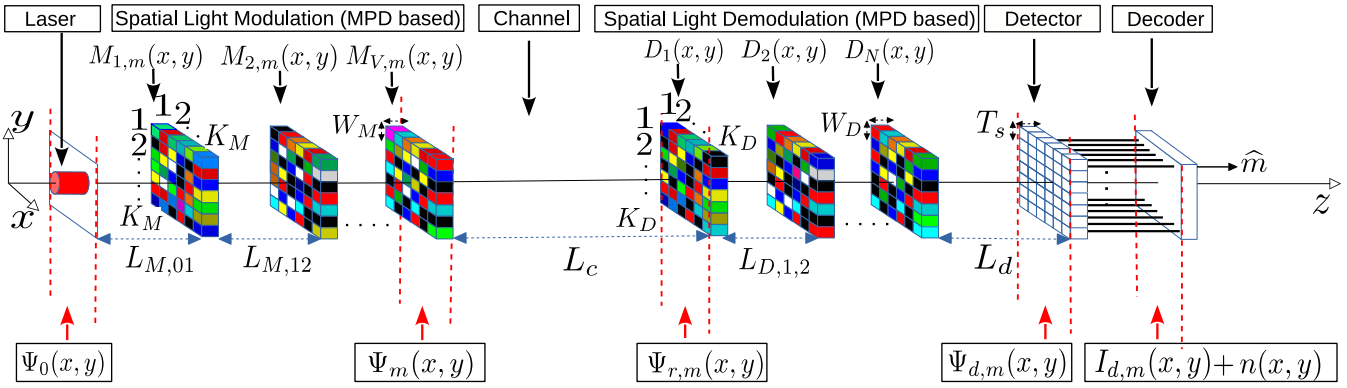

FIGURE 1. 2D spatial light modulation and demodulation design based on MPD where the modulated optical waveform $\Psi_m(x,y)$ for the symbol index m (based on quantum spatial modulation in [17]) propagates through free-space and is demodulated by MPD based demodulator composed of N planes with spatial masks $D_j(x,y)$ for $j \in [1,N]$. $\Psi_{r,m}(x,y)$ at the surface of demodulator is transformed into $\Psi_{d,m}(x,y)$ before intensity detection of $I_{d,m}(x,y)$ and decoding to estimate $\widehat{m}$. Modulation and demodulation are based on V and N planes with distances between jth and $(j+1)$th planes defined as $L_{M,j,j+1}$ and $L_{D,j,j+1}$, respectively. Spatial mask of jth plane of the modulator is denoted by $M_{j,m}(x,y)$ for modulation symbol m.

Furthermore, the following distance metrics are defined for varying $m \in [1,M]$ with a symbol family size of M:

$$d_{min}(m) \equiv \min_{i\in[1,M],\, i\neq m} d_{m,i} \tag{7}$$

$$d_{mean}(m) \equiv \frac{1}{M-1} \sum_{i\in[1,M],\, i\neq m} d_{m,i} \tag{8}$$

$$d_{max}(m) \equiv \max_{i\in[1,M],\, i\neq m} d_{m,i} \tag{9}$$

In addition, mean values with respect to all symbols are defined as follows:

$$\overline{d}_{min} \equiv \frac{1}{M}\sum_{m=1}^{M} d_{min}(m) \tag{10}$$

$$\overline{d}_{mean} \equiv \frac{1}{M}\sum_{m=1}^{M} d_{mean}(m) \tag{11}$$

$$\overline{d}_{max} \equiv \frac{1}{M}\sum_{m=1}^{M} d_{max}(m) \tag{12}$$

In conventional maximum-likelihood detection for AWGN channel model, decision rule is equivalent to finding the transmitted symbol which is closest to the received symbol. Therefore, in the proposed design, demodulated symbols $I_{d,m}[k_x,k_y]$ are analogous to transmitted symbols in simple AWGN models as shown in (2) [33]. Pixel signal-to-noise ratio (SNR) at each PD denoted as SNR_p is defined as P_{av}/σ^2 where P_{av} is average of $I^2_{d,m}[k_x,k_y]$, and each PD has a variance of fixed σ^2. Estimated $\widehat{m}$ minimizes distance as follows:

$$\min_m \left\{ \sum_{k_x=1}^{N_x} \sum_{k_y=1}^{N_y} |y[k_x,k_y] - I_{d,m}[k_x,k_y]|^2 \right\} \tag{13}$$

Next, MPD set-up is modeled with simple rectangular slits for more practical experimental implementation.

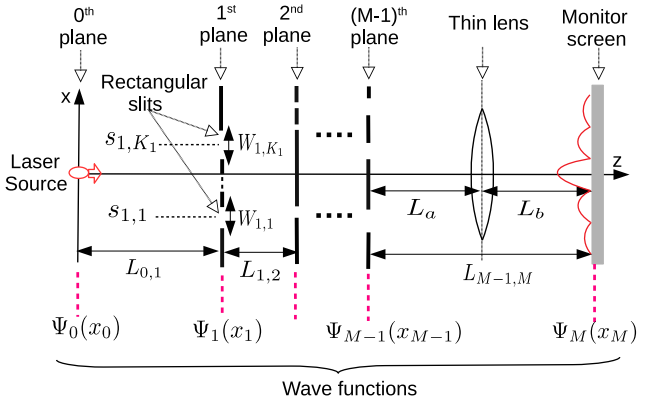

FIGURE 2. Experimental MPD set-up composed of $M-1 = V+N$ diffraction planes with K_j slits on each plane for $j \in [1, M-1]$ and a single sensor plane indexed with M. The central position of kth slit on jth plane is denoted with $s_{j,k}$ and its width is given by $W_{j,k}$. $M-1$ diffraction planes include V modulation and N demodulation planes where the distance between jth and $(j+1)$th planes is denoted with $L_{j,j+1}$.

III. MPD MODELING WITH RECTANGULAR SLITS

MPD design is simplified by using rectangular slits for practical implementation as shown in Fig. 2. In the proposed experimental set-up, there are $M-1 = V+N$ diffraction planes and a final monitor plane while in some scenarios an additional thin lens is utilized after the final diffraction plane. V and N correspond to the number of diffraction planes for modulation and demodulation parts, respectively, as shown in Fig. 1. The plane with index j has K_j slits for $j \in [1, M-1]$ while the kth slit has the central coordinate of $s_{j,k}$ and width $W_{j,k}$ for $k \in [1, K_j]$. The distance between jth and $(j+1)$th planes is denoted with $L_{j,j+1}$ while the distances of the thin lens to the final diffraction and monitor planes are denoted with L_a and L_b, respectively.

The wave function on jth plane is denoted by $\Psi_j(x_j)$ while the source wave function is denoted with $\Psi_0(x_0)$. In this case, the subscript j of $\Psi_j(x_j)$ corresponds to the index of the

TABLE 1. Design parameters for numerical simulation of spatial light modulation and demodulation.

Tx	V	$L_{M,01}$ (mm)	$L_{M,12}$ (mm)	L_c (mm)	Rx	N	$L_{D,12}$ (mm)	$L_{D,23}$ (mm)	L_d (mm)
MPD	2	75	75	950	×	0	×	×	×
				500	SPD	1	×	×	450
				500	MPD	2	50	×	400
				500	MPD	3	50	150	250

plane and x_j denotes the horizontal axis on the surface of jth plane. The source is assumed to be coherent as the output of a standard laser with the source wave function amplitude of light field in one dimension is described as follows:

$$\Psi_0(x_0) = e^{-x_0^2/(2\sigma_0^2)} / \sqrt{\sigma_0 \sqrt{\pi}} \tag{14}$$

where σ_0 is beam width of the Gaussian source wave packet. The relation between the wave functions on jth and $(j+1)$th planes is defined as follows [17]:

$$\Psi_{j+1}\left(x_{j+1}\right) = \int_{-\infty}^{\infty} \Psi_j\left(x_j\right) K\left(x_{j+1}, x_j\right) dx_j \tag{15}$$

where the free space propagation kernel $K(x_{j+1}, x_j)$ is defined as follows for one-dimensional (1D) modeling by using (5):

$$K\left(x_{j+1}, x_j\right) = \frac{e^{\iota\, k\, (x_{j+1}-x_j)^2 / \left(2 L_{j,j+1}\right)}}{\sqrt{\iota\, \lambda\, L_{j,j+1}}} \tag{16}$$

Assume that the phase and amplitude of the light wave propagating through a narrow slit are assumed not to change significantly through the slit, i.e., assuming a fixed value being equal to $\Psi_j(s_{j,k})$ where $s_{j,k}$ is the center of the kth slit on jth plane. Then, the propagating amplitude of the diffracted wave on the next plane through the diffraction due to kth slit is approximated as follows:

$$\Psi_{j+1,k}\left(x_{j+1}\right) \equiv \int_{s_{j,k}^-}^{s_{j,k}^+} \Psi_j\left(s_{j,k}\right) K\left(x_{j+1}, x_j\right) dx_j \tag{17}$$

$$\approx \Psi_j(s_{j,k})\, f\left(s_{j,k}, W_{j,k}, L_{j,j+1}, x_{j+1}\right) \tag{18}$$

where $s_{j,k}^+ = s_{j,k} + W_{j,k}/2$ and $s_{j,k}^- = s_{j,k} - W_{j,k}/2$. The integral of the kernel $f\left(s_{j,k}, W_{j,k}, L_{j,j+1}, x_{j+1}\right)$ through narrow slit is defined as follows:

$$f(s,\, w,\, l,\, x) = \frac{1}{2}\left(\operatorname{erfc}\left(-\frac{\alpha\,(2\,s + w - 2\,x)}{\sqrt{\lambda\, l}}\right) - \operatorname{erfc}\left(-\frac{\alpha\,(2\,s - w - 2\,x)}{\sqrt{\lambda\, l}}\right)\right) \tag{19}$$

where $\operatorname{erfc}(z) \equiv 1 - (2/\sqrt{\pi}) \int_0^z \exp(-t^2)\, dt$ is the complementary error function with complex inputs and $\alpha \equiv (1/2 - \iota/2)\sqrt{\pi/2}$. Then, total wave function amplitude on the $(j+1)$th plane due to diffraction through K_j slits on the jth plane is approximated as follows:

$$\Psi_{j+1}\left(x_{j+1}\right) \approx \sum_{k=1}^{K_j} \Psi_j(s_{j,k})\, f\left(s_{j,k}, W_{j,k}, L_{j,j+1}, x_{j+1}\right) \tag{20}$$

In addition, we divide each single slit into much larger number of narrower slits in order to increase the accuracy in our calculation. The wave function amplitude on the monitor plane is calculated iteratively through each diffraction plane resulting in the following intensity distribution:

$$I\left(x_M\right) \approx \left| \sum_{k=1}^{K_{M-1}} \Psi_{M-1}(s_{M-1,k}) \times f\left(s_{M-1,k}, W_{M-1,k}, L_{M-1,M}, x_M\right) \right|^2 \tag{21}$$

If there is lens after the final plane, the effect of the lens on the input wave function $\Psi_{in}(x)$ is modeled as follows [32]:

$$\Psi_{out}(x) = \Psi_{in}(x)\, e^{-\iota\, \pi\, x^2/(\lambda f_{lens})} \tag{22}$$

where f_{lens} is the focal length of the lens. Therefore, it multiplies the input wave function with the corresponding chirp function depending on the focal length and wavelength. The proposed simplified model with rectangular slits is utilized in experimental implementation in Section V. The general model with both amplitude and phase modulation defined in Section II is utilized for numerical simulation of spatial light demodulation performance in the next section.

IV. NUMERICAL SIMULATION OF SPATIAL LIGHT DEMODULATION

We perform numerical simulation of spatial light demodulation performance in 1D version of the design in Fig. 1 for simplicity for varying number of receiver (Rx) diffraction planes by choosing N between 0 and 2 with parameters as shown in Table 1. MPD based modulation part at Tx is realized with rectangular slits and composed of $V = 2$ planes including nine different combinations of 3, 4 and 5 rectangular slits where distance between the centers of the slits is $D_s = 75$ μm and slit widths are chosen as $W_M = 30$ μm. Therefore, $M_{j,m}(x)$ representing the modulation mask is set as the following:

$$M_{j,m}(x) \equiv \sum_{i=1}^{K_{j,m}} \operatorname{rect}\left(\frac{x - \left(i - (K_{j,m} + 1)/2\right) D_s}{W_M}\right) \tag{23}$$

where $K_{j,m} \in [3, 5]$ denotes the number of slits on jth plane for the modulation index m and the function $\operatorname{rect}(x) = 1$ for $-1/2 \le x \le 1/2$ and otherwise zero. Inter-planar distances of the modulator are chosen as $L_{M,01} = L_{M,12} = 75$ mm. Laser source is chosen with the beam-width $\sigma_0 = 1000$ μm and wavelength $\lambda = 635$ nm. $N_x = 10^5$ PDs are separated with $T_s = 2$ μm at the detector.

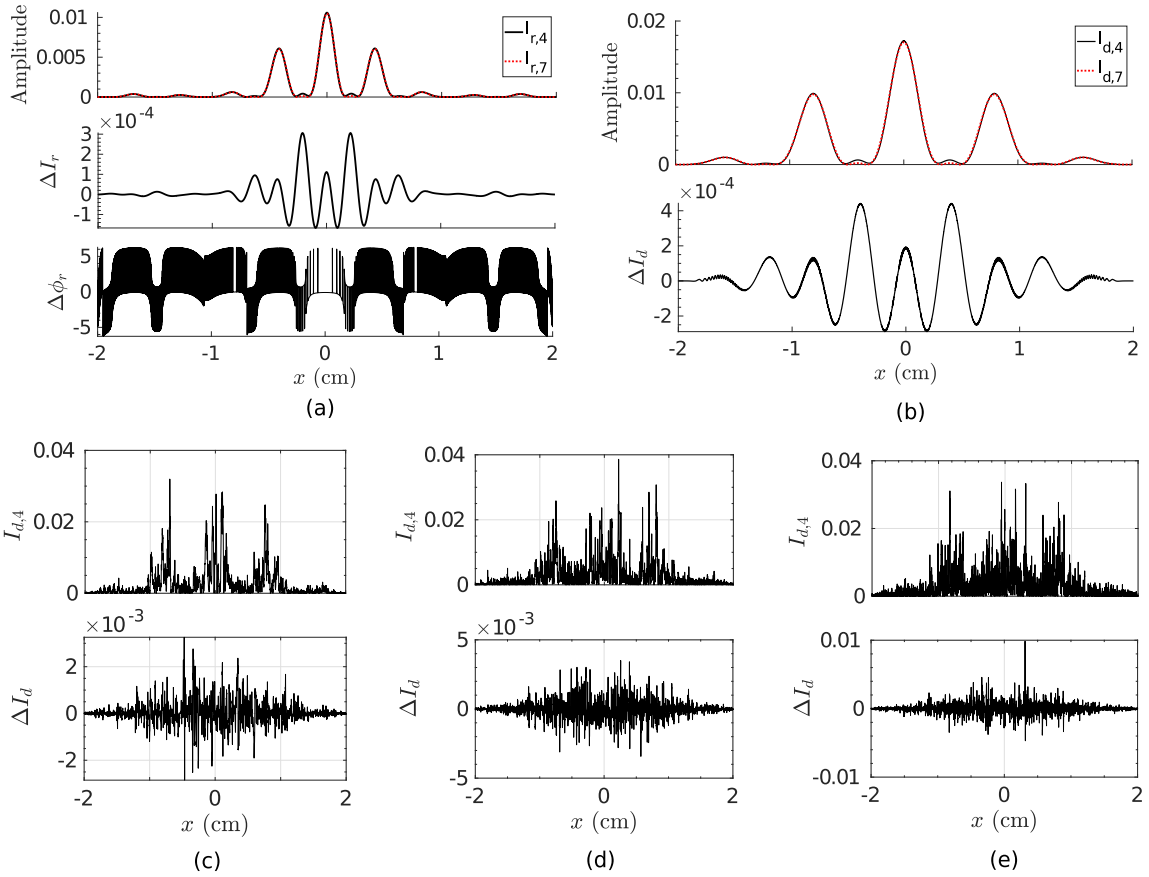

FIGURE 3. Numerical simulation results for intensity distributions of two symbols indexed with $m = 4$ and $m = 7$ are shown for a single trial. (a) Received intensities $I_{r,4}[x]$ and $I_{r,7}[x]$ before applying demodulation, their difference $\Delta I_r[x] = I_{r,4}[x] - I_{r,7}[x]$ and phase difference $\Delta\phi_r[x] = \phi_{r,4}[x] - \phi_{r,7}[x]$. (b) The detected intensities $I_{d,4}[x]$ and $I_{d,7}[x]$ for the case without spatial light demodulator by directly detecting the signal corresponding to $N = 0$ and their difference $\Delta I_d[x] = I_{d,4}[x] - I_{d,7}[x]$. Intensity $I_{d,4}[x]$ for the case with demodulation and the difference $\Delta I_d[x]$ for (c) $N = 1$, (d) $N = 2$ and (e) $N = 3$.

$N = 0$ case denotes the case with direct detection where spatial light demodulation is not applied at Rx. The case $N = 1$ represents state-of-the-art SPD based interferometric demodulation methods while the cases of $N \in \{2, 3\}$ correspond to the MPD based demodulation designs proposed in this article as a proof-of-concept. The extension for $N \geq 4$ is left as a future work. Furthermore, we use phase masking of the form $D_j(x) = e^{\imath\, \phi_{D,j}(x)}$ for $j \in [1, 3]$ to preserve total energy in the demodulated signal compared with the case without spatial light demodulation. Phases in each slit width of $W_D = 50$ μm are modulated by either 0 or π with equal probability by mimicking a pseudo-random noise sequence.

L_d is chosen as 450 mm for $N = 1$ while $L_d + L_{D,12} + L_{D,23} = 450$ mm for $N = 2$ and 3 by making the distance between the first diffraction plane at Rx and the monitor plane equal to 450 mm for both cases. L_c is chosen as 500 mm for the cases with demodulation for an example of short-range communication channel while $L_c = 450\,\text{mm} + 500\,\text{mm} = 950$ mm for the case without demodulation by making the distance between modulator part and the monitor plane the same for both the cases with and without spatial light demodulation.

Each symbol power is normalized by setting $r_e P_m$ so that total squared intensity at PD array is unity for $m \in [1, 9]$ by satisfying $||\mathbf{I}_{d,m}||^2 = \sum_{k_x} I_{d,m}^2[k_x] = 1$ where $I_{d,m}[k_x] \approx r_e P_m T_s |\Psi_{d,m}(k_x T_s)|^2$. The symbols are indexed with $m \in [1, 9]$ for 9 different combinations of $[K_{1,m}\ K_{2,m}]$. In the following discussion, $I_{d,m}[x]$ denotes the sampled value corresponding to $x = k_x T_s$. Therefore, $I_{val}[x]$ and $\phi_{val}[x]$ are used instead of $I_{val}[k_x]$ and $\phi_{val}[k_x]$, respectively, where $\{val\}$ denotes $\{d\}$, $\{d, m\}$, $\{r\}$ or $\{r, m\}$ for varying symbol index m.

The minimum, average and maximum inter-symbol distances are denoted with $d_{min}(m)$, $d_{mean}(m)$ and $d_{max}(m)$, respectively, for each symbol m for varying N values. The total number of trials is chosen as 10 while the performance is calculated by getting average of the distances in 10 trials with random phase masks $D_j(x)$ for $j \in [1, 3]$ in each trial. Increasing the number of trials is left as a future work due to computational constraints while providing a reliable observation as a proof-of-concept. In Fig. 3, intensity distributions of specific symbols are shown for a single trial to analyze the effect of spatial light demodulation. The minimum of d_{min} occurs between $m = 4$ and $m = 7$ corresponding to

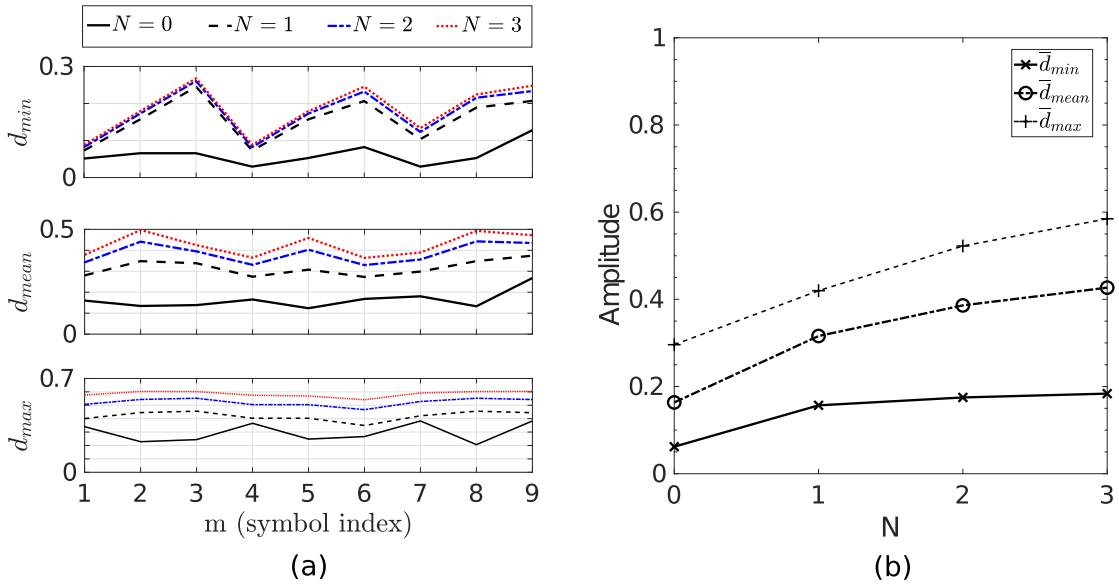

FIGURE 4. Numerical simulation based performance comparison between direct detection for $N = 0$ and spatial light demodulation for $N = 1$ and $N \in \{2, 3\}$ corresponding to SPD and MPD, respectively. (a) $d_{min}(m)$, $d_{mean}(m)$ and $d_{max}(m)$ correspond to minimum, mean and maximum inter-symbol distances, respectively, for each symbol index $m \in [1, 9]$. (b) $\bar{d}_{min}$, $\bar{d}_{mean}$ and $\bar{d}_{max}$ denoting average values of $d_{min}(m)$, $d_{mean}(m)$ and $d_{max}(m)$, respectively, for $m \in [1, 9]$ are shown for varying N. Average inter-symbol distance increases with increasing N as a proof-of-concept for MPD based spatial light demodulation advantages.

$\left[K_{1,m}\ K_{2,m}\right] = [4\ 3]$ and $[5\ 3]$, respectively, for the case $N = 0$ without spatial light demodulation. $I_{r,4}[x]$ and $I_{r,7}[x]$ with their amplitude and phase differences defined as $\Delta I_r[x] \equiv I_{r,4}[x] - I_{r,7}[x]$ and $\Delta\phi_r[x] \equiv \phi_{r,4}[x] - \phi_{r,7}[x]$, respectively, are shown in Fig. 3(a). Observe that there is a high-frequency phase difference oscillation between different symbols while with similar intensities. Detected $I_{d,4}[x]$ and $I_{d,7}[x]$ and their difference $\Delta I_d[x] \equiv I_{d,4}[x] - I_{d,7}[x]$ for the case without demodulation are shown in Fig. 3(b) with the observations of highly similar intensities and difficulty to decode. In spatial light demodulation, phase difference is exploited with random phase masks to obtain highly interfering diffraction patterns for $N = 1, 2$ and 3 as shown in Figs. 3(c), (d) and (e), respectively. The difference $\Delta I_d[x]$ increases with increasing values of N resulting in an increased decoding performance.

It is observed in Fig. 4(a) that spatial light demodulation increases distances significantly for increasing values of N for all symbol indices $m \in [1, 9]$. In Fig. 4(b), the distances are calculated by using (10–12) where the average for all symbol values is calculated, i.e., $\bar{d}_{val} \equiv (1/9) \sum_{m=1}^{9} d_{val}(m)$, for $N \in [0, 2]$ where *val* corresponds to either *min*, *mean* or *max*. All distance values increase with increasing values of N by improving inter-symbol distance at the detector front-end ≈ 2 times at maximum. It is a future work to extend the analysis to larger symbol families and higher values of N.

V. EXPERIMENTAL RESULTS

SPD and the proposed MPD system for spatial light modulation and demodulation are experimentally realized with the optical set-up in Fig. 5(a) where its design is shown in Fig. 5(b). Experiments are based on the practical design shown in Fig. 2 with rectangular slits where the corresponding parameters including set-up identification (ID) numbers, the types of diffraction at Tx and Rx, the total number of diffraction planes $M - 1 = V + N$, the number of diffraction planes V and N for Tx and Rx, respectively, the number of slits in each plane K_j for $j \in [1, 4]$, inter-planar distances $L_{j,j+1}$ for $j \in [0, 4]$, whether final lens is utilized, focal length f_{lens} of the lens in centimeters and the distance parameters L_a and L_b of the lens are presented in Table 2. The plates including rectangular slits are freely moved along x and z axis with micrometer accuracy based on adjustable holding system. The positions of the plates are adjusted by using a rail mechanism allowing to modify inter-planar distances. The monitor plane is composed of black paper reflecting the diffracted wave such that its photo allows to extract the intensity distribution. All the photographs of monitor plane are obtained in total darkness in order to remove the effect of background light. Smart phone camera (Iphone SE 2020) is used to capture the images.

Gaussian laser source with wavelength $\lambda = 635$ nm and beam-width $\sigma_0 = 1000$ μm is utilized where the power of the compact laser module is 0.91 mW (Thorlabs). Diffraction slits are realized either by using metallic coated glass plates (3B Scientific) as shown in Figs. 5(c), (d) and (e) or manufactured with a low-cost design by placing graphite cylinders with diameters of 300 μm on glass plates as shown in Figs. 5(f), (g), (h) and (i). Metallic coated glass plates include uniformly distributed slit positions with varying numbers of

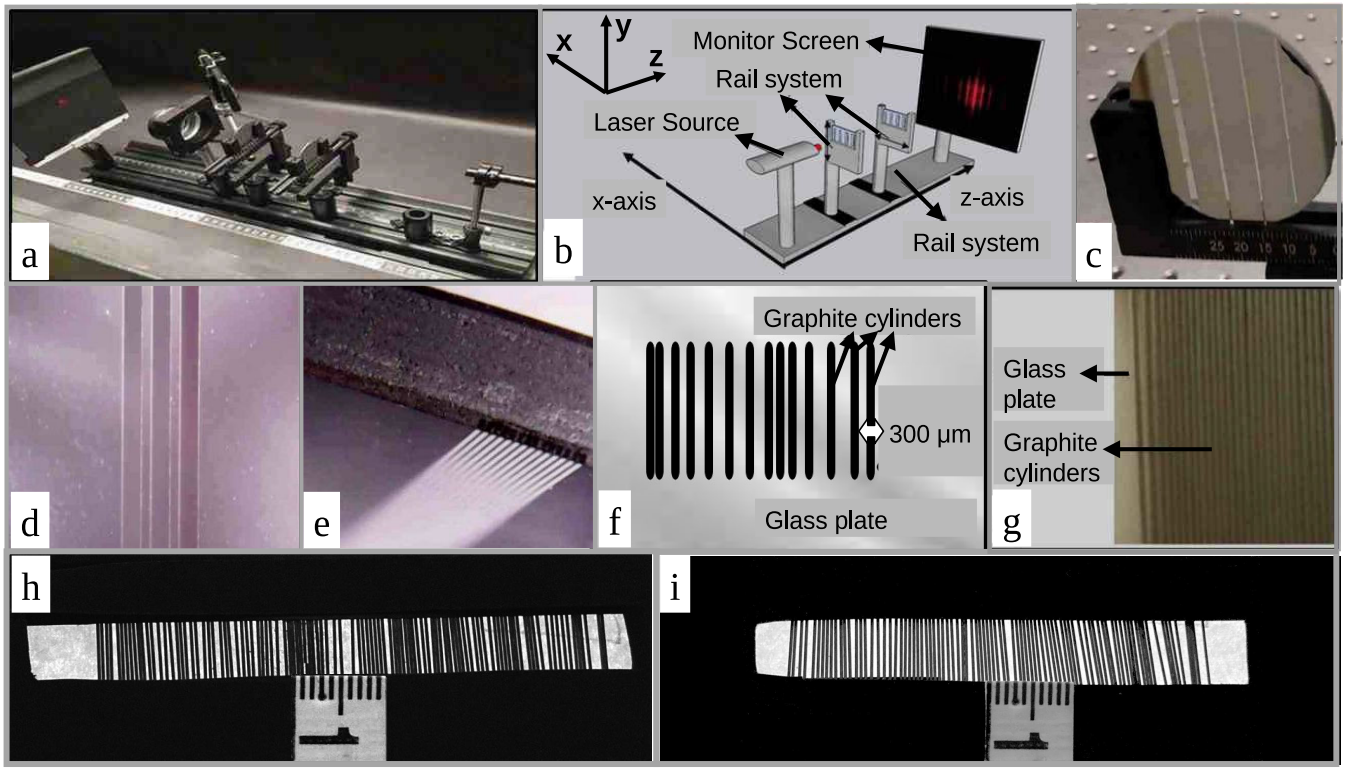

FIGURE 5. (a) Implementation set-up of the experimental MPD system. b) 3D design of MPD system where the arrows indicate the capability of movement for plates in both x and z axes. c) Photo of a single diffraction plate formed by lithography of metallic coated glass plate showing four different groups of the slits with the number of slits being equal to 14, 6, 4 and 3 from left to the right (3B Scientific). Each slit width and the distance between neighbour slits are equal to 40 μm and 100 μm, respectively. (d) The front view of the triple slit on the glass plate and (e) the side view of 14 slits on the glass plate. (f) Modeling of practical slit obtained by random placement of graphite cylinders with radius 300 μm by creating a random distribution of multiple slits with varying width. (g) The photo of a practical slit realized with graphite cylinders. (h) and (i) Photos of two slit plates based on the design in (f) with randomly distributed graphite cylinders where the width of the scale bar at the center is 1 cm composed of mm scale tick marks. These plates are utilized in Section V-D for spatial light demodulation experiments with two plates.

3, 4, 6 and 14 as shown in Fig. 5(c). Each slit has fixed width of 40 μm and the distance between neighbor slit centers is equal to 100 μm. On the other hand, modeling of the manufactured diffraction plate is shown in Fig. 5(f). Two plates utilized for experimental studies in Section V-D are shown in Figs. 5(h) and (i) where total number of graphite based slits is larger than 20 while their thickness values and positions are random due to the simplified manufacturing method by directly attaching them on the glass plate.

There are 36 different kinds of experiments performed with the following set-up ID numbers and definitions:

- S1 to S8: Spatial light modulation with SPD based Tx
- S9 to S12: Spatial light modulation with MPD based Tx
- S13 to S20: Spatial light modulation with MPD based Tx and demodulation with direct detection at Rx
- S21 to S28: Spatial light modulation with MPD based Tx and demodulation with SPD based Rx
- S29 to S36: Spatial light modulation with MPD based Tx and demodulation with MPD based Rx

Spatial light demodulation is performed with random slits manufactured by using graphite cylinders as shown in Figs. 5(h) and (i). Concave lens with focal length of $f_{lens} = -7.5$ cm is utilized in set-up IDs of S5, S6, S7 and S8 in order to obtain patterns with magnified details at the central spatial region for SPD experiments. Next, image processing methods to transform the captured images of light diffraction into intensity distributions are presented.

A. IMAGE PROCESSING METHODS

Images of the intensity pattern on the monitor plane are captured with the camera. After the laser diffracts through the slits, the captured image of the pattern appearing on the monitor is denoted as raw image as shown in the first step in Fig. 6. Photos are captured from the side but not directly in front of the monitor screen. Therefore, there is perspective distortion in the acquired raw image. Warping operation is applied to correct the distortion by obtaining $M \times N$ pixels image data. Then, the color image is converted to gray-scale intensity values denoted with matrix A with values $A[x, y]$ along the pixel locations (x, y) by using black and white (BW) filtering. Since the diffraction slits are 1D with lengths of several centimeters along y axis and microscale widths along x axis, the resulting intensity values are summed along y axis vertically in order to obtain 1D intensity distribution denoted with $I_{exp}[x]$ along x axis while each x value corresponds to the

TABLE 2. Parameters of 36 different experimental set-ups for spatial light modulation and demodulation based on rectangular slits.

ID	Tx	Rx	$M-1$	V	N	K_1	K_2	K_3	K_4	f_{lens} (cm)	L_{01} (cm)	L_{12} (cm)	L_{23} (cm)	L_{34} (cm)	L_{45} (cm)	L_a (cm)	L_b (cm)
S1	SPD	×	1	1	0	3	×	×	×	×	11	113	×	×	×	×	×
S2	SPD	×	1	1	0	4	×	×	×	×	11	113	×	×	×	×	×
S3	SPD	×	1	1	0	6	×	×	×	×	11	113	×	×	×	×	×
S4	SPD	×	1	1	0	14	×	×	×	×	11	113	×	×	×	×	×
S5	SPD	×	1	1	0	3	×	×	×	−7.5	11	113	×	×	×	19	94
S6	SPD	×	1	1	0	4	×	×	×	−7.5	11	113	×	×	×	19	94
S7	SPD	×	1	1	0	6	×	×	×	−7.5	11	113	×	×	×	19	94
S8	SPD	×	1	1	0	14	×	×	×	−7.5	11	113	×	×	×	19	94
S9	MPD	×	2	2	0	3	3	×	×	×	4	4	116	×	×	×	×
S10	MPD	×	2	2	0	4	3	×	×	×	4	4	116	×	×	×	×
S11	MPD	×	2	2	0	6	3	×	×	×	4	4	116	×	×	×	×
S12	MPD	×	2	2	0	6	4	×	×	×	4	4	116	×	×	×	×
S13	MPD	×	2	2	0	3	4	×	×	×	4	8	126	×	×	×	×
S14	MPD	×	2	2	0	3	6	×	×	×	4	8	126	×	×	×	×
S15	MPD	×	2	2	0	4	3	×	×	×	4	8	126	×	×	×	×
S16	MPD	×	2	2	0	4	4	×	×	×	4	8	126	×	×	×	×
S17	MPD	×	2	2	0	4	6	×	×	×	4	8	126	×	×	×	×
S18	MPD	×	2	2	0	6	3	×	×	×	4	8	126	×	×	×	×
S19	MPD	×	2	2	0	6	4	×	×	×	4	8	126	×	×	×	×
S20	MPD	×	2	2	0	14	4	×	×	×	4	8	126	×	×	×	×
S21	MPD	SPD	3	2	1	3	4	>20	×	×	4	8	86	40	×	×	×
S22	MPD	SPD	3	2	1	3	6	>20	×	×	4	8	86	40	×	×	×
S23	MPD	SPD	3	2	1	4	3	>20	×	×	4	8	86	40	×	×	×
S24	MPD	SPD	3	2	1	4	4	>20	×	×	4	8	86	40	×	×	×
S25	MPD	SPD	3	2	1	4	6	>20	×	×	4	8	86	40	×	×	×
S26	MPD	SPD	3	2	1	6	3	>20	×	×	4	8	86	40	×	×	×
S27	MPD	SPD	3	2	1	6	4	>20	×	×	4	8	86	40	×	×	×
S28	MPD	SPD	3	2	1	14	4	>20	×	×	4	8	86	40	×	×	×
S29	MPD	MPD	4	2	2	3	4	>20	>20	×	4	8	31	55	40	×	×
S30	MPD	MPD	4	2	2	3	6	>20	>20	×	4	8	31	55	40	×	×
S31	MPD	MPD	4	2	2	4	3	>20	>20	×	4	8	31	55	40	×	×
S32	MPD	MPD	4	2	2	4	4	>20	>20	×	4	8	31	55	40	×	×
S33	MPD	MPD	4	2	2	4	6	>20	>20	×	4	8	31	55	40	×	×
S34	MPD	MPD	4	2	2	6	3	>20	>20	×	4	8	31	55	40	×	×
S35	MPD	MPD	4	2	2	6	4	>20	>20	×	4	8	31	55	40	×	×
S36	MPD	MPD	4	2	2	14	4	>20	>20	×	4	8	31	55	40	×	×

discrete pixel location $k_x\ T_s$ with a similar notation in Sec. IV. Since the images are taken with camera and the range of the intensity levels which can be captured are limited, intensity saturation is observed depending on the power level of the laser source. Therefore, intensity levels are normalized for different regions around peak values based on theoretically calculated maximum values for each region, i.e., for each R_i for $i \in [1, 4]$. Resulting normalized intensity distribution is denoted with $I_{exp,n}[x]$. Raw images for set-up IDs S2, S3, S5 and S8, are shown in Figs. 7(a), (b), (c) and (d), respectively, for SPD while MPD raw images are shown Figs. 7(e) and (f), for S10 and S12, respectively. White regions at the center of the diffraction patterns at the middle of the main peak in Figs. 7(a) and (b) indicate high levels of intensity saturation while smaller level saturation is observed in Figs. 7(c), (d), (e) and (f). Next, image processing steps are explained in detail.

1) WARPING

It is not possible to place the camera exactly in front of the screen since the laser light is blocked as seen in Fig. 5(a). Four corners of the plane is chosen to make projective transformation via MATLAB for realizing perspective correction. Since the images are taken in totally dark environment, glowing phosphors are used to determine four corners of the plane. After this step, an image is obtained as if the camera is positioned in front of the screen as shown in Fig. 6. Warping process decreases the resolution of the warped image to 1600×900 pixels expressed as $M \times N$ in Fig. 6 although the size of the raw image is 4032×2268 pixels.

2) IMAGE FILTERING

Threshold levels are applied on warped images to set the maximum and minimum levels of intensity values. Maximum

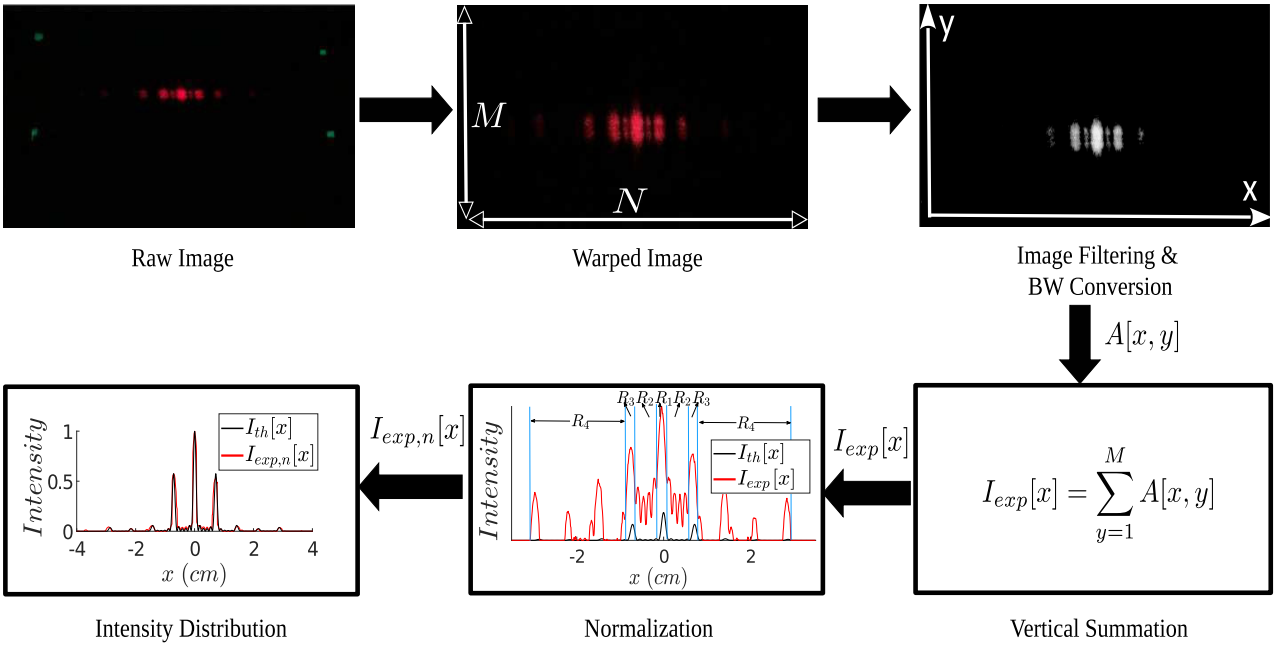

FIGURE 6. Image processing steps showing warping, BW filtering, vertical summation, normalization and final intensity distribution.

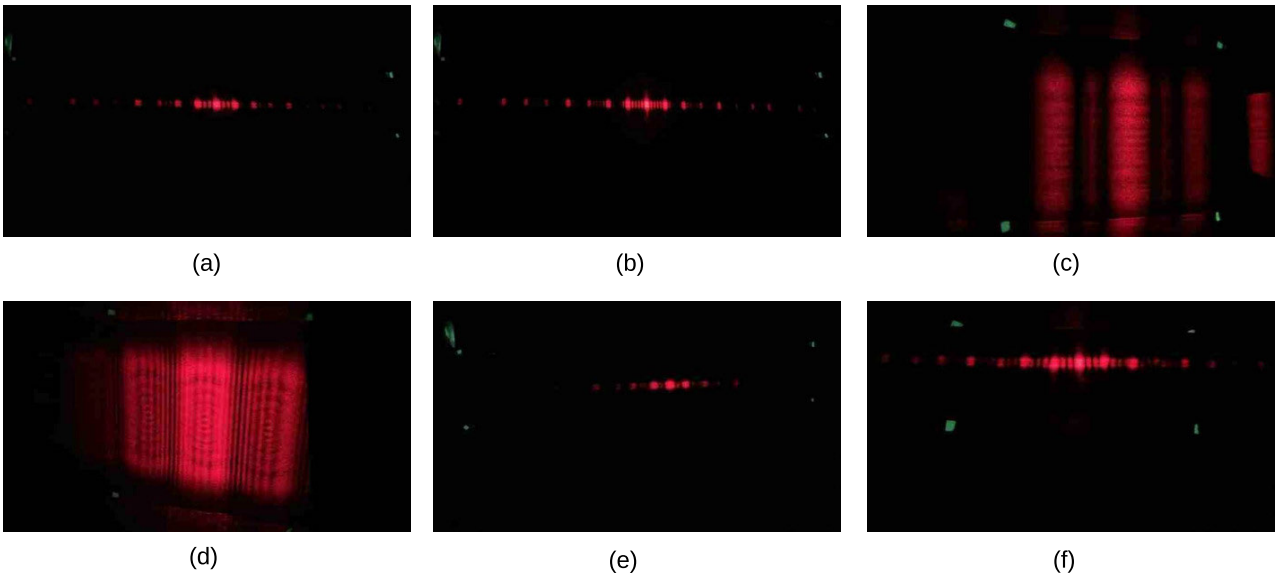

FIGURE 7. Raw images displayed on monitor plane after the laser beam diffracts through different set-ups where the rectangular boundary of the active area is determined by using glowing phosphorescence material shown with green dots in the pictures. Captured images are shown for set-up IDs (a) S2, (b) S3, (c) S5, (d) S8, (e) S10 and (f) S12.

threshold values are manually adjusted for each image to the highest intensity levels to avoid saturation while minimum threshold values are set the lowest possible levels. Intensity patterns on the monitor are transformed to BW monochrome images as shown in Fig. 6. Then, intensity values of gray-scale images are saved as a 2D matrix $A[x, y]$ of size $M \times N$ where M is the number of rows and N is the number of columns.

3) VERTICAL SUMMATION

Diffraction slits utilized in experimental studies are designed for 1D diffraction studies. The slits extend along y axis for several centimeters while having microscale widths along x axis. Therefore, the resulting intensity values are summed along y axis vertically to obtain 1D intensity distribution $I_{exp}[x]$ along x axis as follows:

$$I_{exp}[x] = \sum_{y=1}^{M} A[x, y] \tag{24}$$

4) NORMALIZATION

Captured images show saturation while not supporting the exact intensity scale of the spatial distribution of the number of photons. For example, if the number of photons is

larger than some specific threshold level, then its intensity is transformed into pure white color in the acquired BW image with maximum intensity level, e.g., 255 for the scale of [0, 255], irrespective of the exact level of the light intensity. Therefore, the levels of peaks for different spatial regions of the distribution need to be rescaled either by using different source intensities or by normalizing with respect to the maximum theoretical values in each region. Spatial regions of the intensity distribution are divided into four different regions denoted with R_1, R_2, R_3 and R_4 along x axis as shown in Fig. 6. Then, normalizing coefficients C_i in each region R_i for $i \in [1, 4]$ are calculated as follows:

$$C_i = \left(\max_{x \in R_i} I_{th}[x]\right) / \left(\max_{x \in R_i} I_{exp}[x]\right) \quad (25)$$

$$I_{exp,n}[x] = C_i I_{exp}[x] \text{ for } x \in R_i \quad (26)$$

where $I_{th}[x]$ and $I_{exp}[x]$ are theoretical and experimental intensity distributions, respectively, and $I_{exp,n}[x]$ is the normalized experimental intensity distribution. $I_{th}[x]$ is calculated based on theoretical formulations in (21) and (22) for free space propagation of wave function and lens based masking, respectively. Its maximum is normalized to unity for better comparison with experimental results. After the normalization process, theoretical and experimental intensity distributions are much more compatible as shown in the last step of Fig. 6. Besides that, if only the central peaks are normalized as in the experiments with lens for set-up IDs S5, S6, S7 and S8, then the intensity on the monitor plane is denoted with $\widetilde{I}_{exp}[x]$ in order to discriminate from unnormalized $I_{exp}[x]$.

B. SPATIAL LIGHT MODULATION WITH SINGLE PLANE DIFFRACTION

Experimental results for spatial light modulation with SPD based transmitter for increasing number of slits with values 3, 4, 6 and 14 are shown in Figs. 8(a), (b), (c) and (d), respectively, for the case without lens while the cases with concave lens are shown in Figs. 8(e), (f), (g) and (h), respectively. Theoretical distributions $I_{th}[x]$ numerically calculated based on formulations in (21) and (22) and experimental results are observed to be quite similar where peak locations are significantly in agreement even for side lobes. The number of side-lobe peaks increases with the increasing number of slits as observed in Figs. 8(a) and (d). Resolution of camera is not sufficient for observing the results in Figs. 8(c) and (d) in more detail where details around the central region cannot be accurately detected. Concave lens is used to overcome this problem by allowing a wider view of intensity distribution with increased resolution. As the laser beam propagates through concave lens, intensity of diffracted laser beam is decreased by also reducing the negative effects of saturation. Intensity distributions for theoretical and experimental results are highly similar as shown in Figs. 8(e), (f), (g) and (h) even without normalization along different regions except the central peak. Set-up S8 with 14 slits provides intensity distribution with highest oscillation frequency as shown in Fig. 8(h) while in agreement with theoretical calculations.

C. SPATIAL LIGHT MODULATION WITH MULTI-PLANE DIFFRACTION

MPD based modulation experiments corresponding to set-up IDs between S9 and S12 are performed for varying slit pairs of $[K_1\ K_2]$ with values of [3 3], [4 3], [6 3] and [6 4] as shown in Figs. 9(a), (b), (c) and (d), respectively, while generating different symbols for modulation operation. It is observed that theoretical and experimental results for MPD are in agreement. The distance L_{12} and the pairs of $[K_1,\ K_2]$ are chosen with trial and error to maximize the variation compared with SPD case having the same L_{01} and K_1. Intensity of diffracted laser beam decreases more compared with SPD reducing the effect of saturation. Therefore, peak intensity levels of theoretical and experimental results are very close to each other. It is observed that increasing the number of slits in both plates results in an increase in spatial frequency, e.g., two peaks between the main and side lobes as shown in Fig. 9(d).

D. SPATIAL LIGHT DEMODULATION WITH MULTI-PLANE DIFFRACTION

Spatial light demodulation is experimentally realized for eight different symbols for simplicity and as a proof-of-concept in a similar manner to the simulation studies in Section IV. Each symbol corresponds to a different combination of the number of slits K_1 and K_2 on the first and second modulation planes, respectively, as shown in Table 2. The case without spatial light demodulation for $N = 0$ is compared with the cases exploiting spatial light demodulation for $N = 1$ and $N = 2$ for the same pairs of K_1 and K_2 corresponding to different symbols. $[K_1\ K_2]$ corresponds to [3 4], [3 6], [4 3], [4 4], [4 6], [6 3], [6 4] and [14 4] for eight different symbols where the detected symbol intensities at the detector array are denoted with $I_{d,m}$ for $m \in [1, 8]$. They are normalized in a similar manner with the simulation studies where $||\mathbf{I}_{d,m}||^2 = 1$ for $m \in [1, 3]$. Demodulation methods with $N = 0$, $N = 1$ and $N = 2$ are experimented with set-up IDs in the intervals of [S13, S20], [S21, S28] and [S29, S36], respectively.

Processed images of the detected symbols after image filtering and BW conversion are shown in Figs. 10(a), (b) and (c) for $N = 0$, $N = 1$ and $N = 2$, respectively. Intensity distributions of the power normalized symbols after vertical summation, i.e., $||\mathbf{I}_{d,m}||^2 = \sum_{k_x} I^2_{d,m}[k_x] = 1$ for $m \in [1, 8]$, are shown in Figs. 11(a), (b) and (c) for $N = 0$, $N = 1$ and $N = 2$, respectively. It is observed in Figs. 11(b) and (c) for $N = 1$ and $N = 2$, respectively, that as N increases the patterns appear as more randomized and having higher frequency compared with smooth distributions shown in Fig. 11(a). Similarity comparison among symbol intensity patterns is achieved by using inter-symbol distance definition in (6) which is the fundamental mechanism utilized for maximum-likelihood detection as discussed in Section II [33]. The resulting

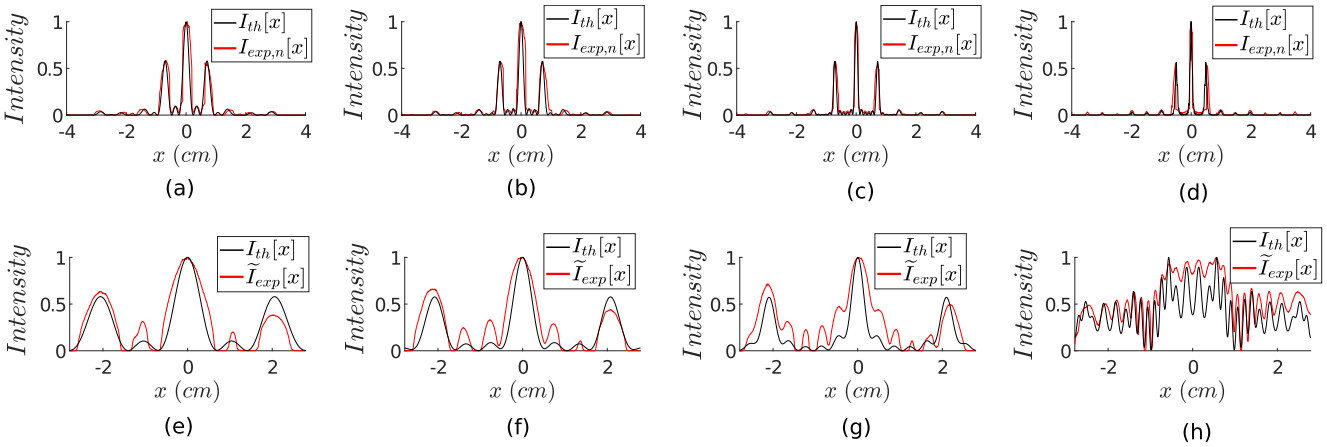

FIGURE 8. The comparison of $I_{th}[x]$ numerically calculated based on theoretical formulations in (21) and (22) and normalized experimental intensity measurements $I_{exp,n}[x]$ based on (26) and $\tilde{I}_{exp}[x]$ based on the maximum value of $I_{th}[x]$ for SPD experiments with set-up IDs a) S1, b) S2, c) S3, d) S4, e) S5, f) S6, g) S7 and h) S8.

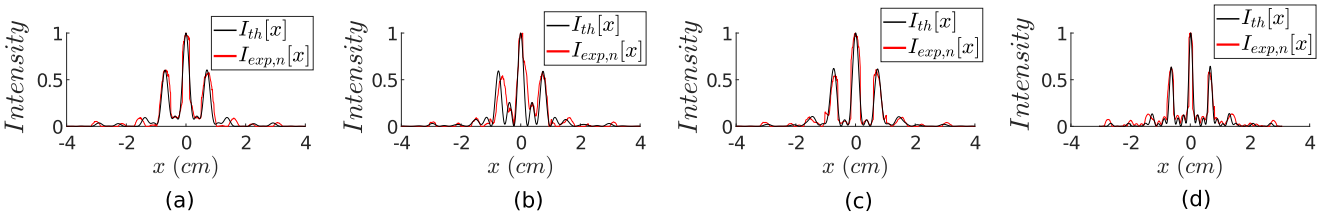

FIGURE 9. The comparison of $I_{th}[x]$ numerically calculated based on theoretical formulation in (21) and normalized experimental intensity measurements $I_{exp,n}[x]$ based on (26) for MPD experiments with set-up IDs (a) S9, (b) S10, (c) S11 and (d) S12.

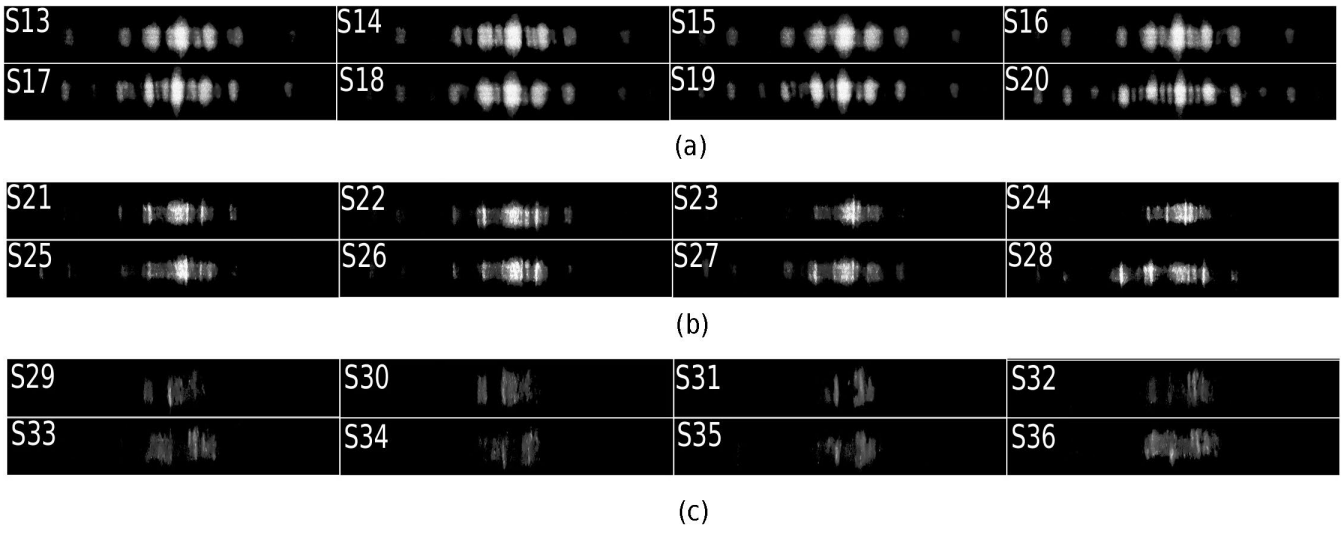

FIGURE 10. Processed images for intensity distributions of eight symbols corresponding to set-up IDs (a) between S13 and S20 for $N = 0$, (b) between S21 and S28 for $N = 1$ and (c) between S29 and S36 for $N = 2$ after image filtering and BW conversion.

experimental inter-symbol distances $d_{min}(m)$, $d_{mean}(m)$ and $d_{max}(m)$ are shown in Figs. 12 (a), (b) and (c), respectively, for varying symbol indices $m \in [1, 8]$. It is observed that MPD based spatial light demodulation improves $d_{min}(m)$, $d_{mean}(m)$ and $d_{max}(m)$ for increasing values of N for all symbol indices. In Fig. 12(d), $\overline{d}_{min}$, $\overline{d}_{mean}$, and $\overline{d}_{max}$ for $N \in [0, 2]$ are shown based on the average values with respect to all symbols. It is observed that mean distance values $\overline{d}_{min}$, $\overline{d}_{mean}$ and $\overline{d}_{max}$ increase with increasing values of N, e.g., approximately two times improvement with $N = 2$ similar to the simulation results in Section IV for simple modulation symbols as an experimental proof-of-concept. It is a future

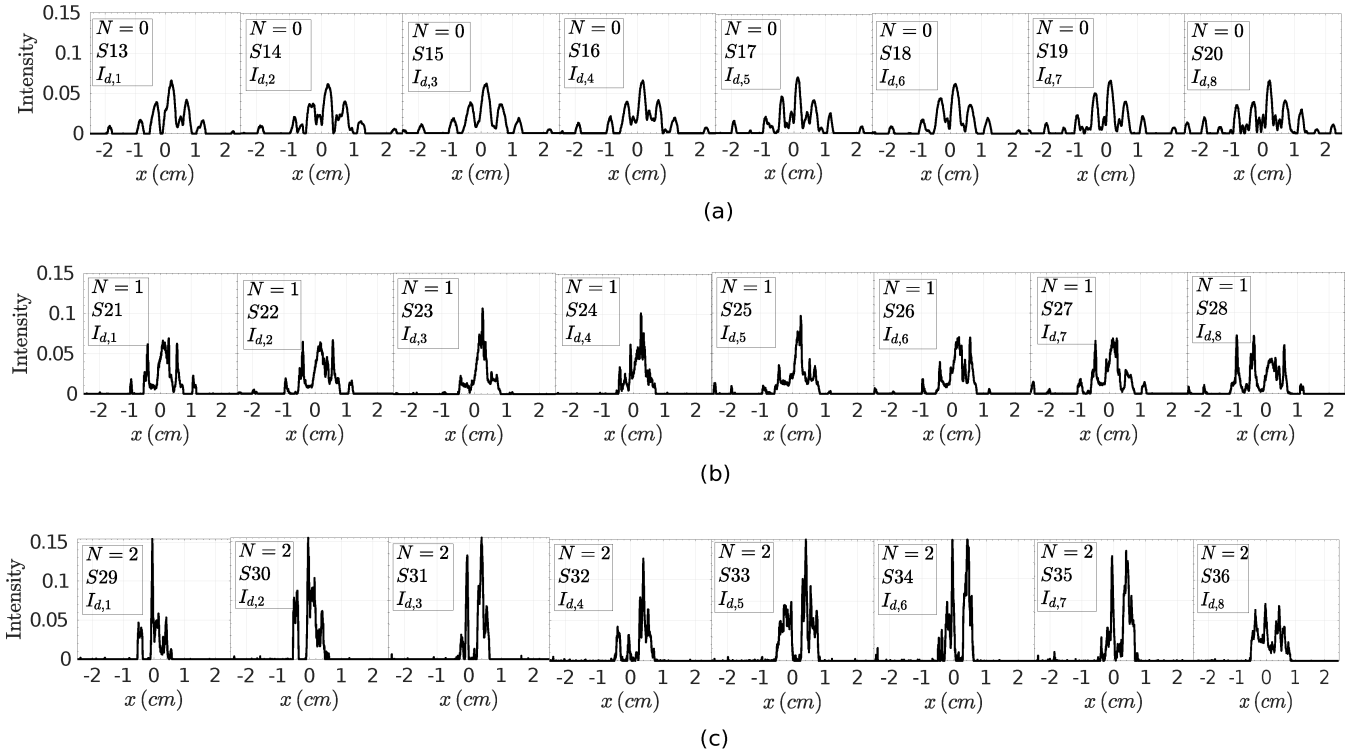

FIGURE 11. Intensity distributions of detected eight symbols after vertical summation corresponding to set-up IDs (a) between S13 and S20 for $N = 0$, (b) between S21 and S28 for $N = 1$ and (c) between S29 and S36 for $N = 2$. $I_{d,m}$ denotes the detected symbol symbol intensity for mth symbol while each of them is normalized to satisfy $||\mathbf{I}_{d,m}||^2 = \sum_{k_x} I^2_{d,m}[k_x] = 1$ while without any normalization based on the theoretical values for fair comparison among different N values with plates composed of randomly distributed slits.

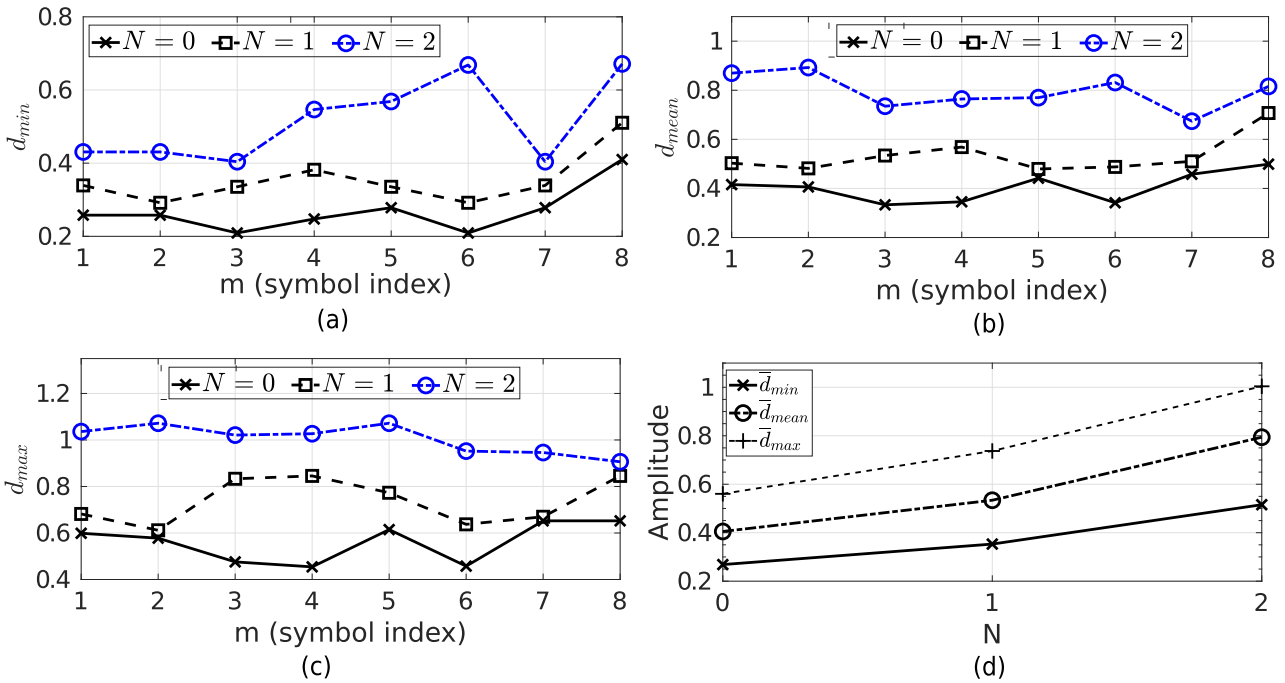

FIGURE 12. Experimental performance comparison between demodulation based on direct detection for $N = 0$ and spatial light demodulations for $N = 1$ and $N = 2$ corresponding to SPD and MPD, respectively. (a) $d_{min}(m)$, (b) $d_{mean}(m)$ and (c) $d_{max}(m)$ correspond to minimum, mean and maximum inter-symbol distances, respectively, for each symbol index $m \in [1, 8]$. (d) $\bar{d}_{min}$, $\bar{d}_{mean}$ and $\bar{d}_{max}$ denoting average values of $d_{min}(m)$, $d_{mean}(m)$ and $d_{max}(m)$, respectively, for $m \in [1, 8]$ are shown for varying N.

work to experiment with much larger number of slits and planes in both modulation and demodulation parts in order to observe the advantages for significantly higher order symbol families.

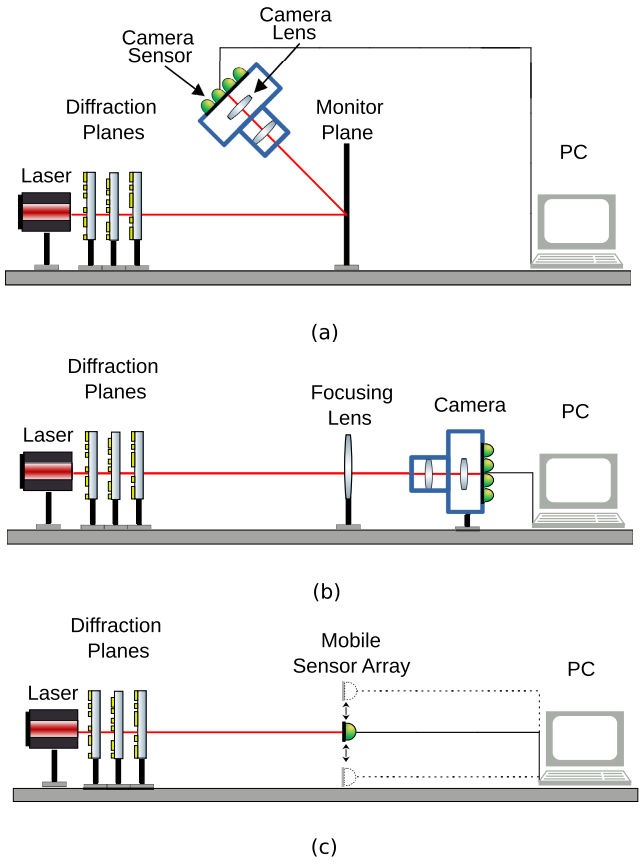

FIGURE 13. Detector architectures for diffraction patterns (a) by taking photos of the light reflected from monitor plane in total darkness, (b) by using CCD or CMOS based camera receiver with fixed position where the pattern is focused on the imaging pixel area of the camera, and (c) by using mobile sensor array where the position of the sensor is mechanically adjusted to cover the large area of the diffraction pattern especially for ultra-low light levels with single photon detectors.

Next, experimental challenges for the proposed design and future works to further improve the experimental accuracy are discussed.

E. EXPERIMENTAL CHALLENGES AND FUTURE WORKS

Three different designs for interference pattern measurement are shown in Fig. 13. The design in Fig. 13(a) is utilized in experimental studies in this article based on measurement of the reflected light from monitor screen in total darkness while the designs in Figs. 13(b) and (c) utilize direct detection of the incoming light as discussed in Section V-E2. In this article, the design shown in Fig. 13(a) is utilized with the following motivation as discussed next while the challenges are discussed in Section V-E1.

Fundamental target in this article is to compare theoretical calculations and experimental measurements for MPD based spatial modulation system design originally defined without any lens in [17] and for large communications distances. We design our experiments for large inter-planar distances on the order of tens of centimeters resulting in large area diffraction patterns requiring additional external lens to focus for detection with camera lenses. The overall system is regarded as a Fourier optics system where the effects of free space and lens on the propagating wave function are theoretically modeled in (16) and (22), respectively. The comparison of theory and experiment for MPD design without external focusing lens is performed to accurately compare the effect of MPD on the wave function for freely propagating wave function. A low-complexity measurement architecture without any external lens is presented for large are diffraction patterns due to long distance communications. As a result, monitor screen based measurement is a low complexity and alternative method fundamentally similar to the camera sensor based measurement in Fig. 13(b) while with various experimental challenges due to the design not utilizing any external lens in total darkness and directly exploiting the reflected light from monitor screen as discussed in Section V-E1. Performed measurements are accurate enough to verify the advantages of spatial light modulation as one of the main targets of the presented article.

1) EXPERIMENTAL CHALLENGES

Firstly, the resolution of the camera is limited to 4032×2268 pixels while the active area after warping where the pattern is observed is decreased to 1600×900 pixels. Increasing the resolution of camera and dynamic range for reducing the effect of saturation is an open issue to obtain more accurate intensity distributions not only for monitor screen based solution but also for camera sensor based solution in Fig. 13(b).

Secondly, camera is placed at the side of the monitor plane resulting in perspective distortion. Image warping is applied to correct perspective distortion leading to errors at the positions of the peaks and their amplitudes. Glowing phosphors are used to distinguish the four corner points for the image warping process. There are minor errors for warping process itself due to larger size of phosphors and resolution of the camera. Implementing experimental design with smaller phosphors and higher resolution camera improves the accuracy of the experimental measurements as an open issue.

After normalization process, distance between theoretical expectations and experimental results is calculated by using the following distance definition:

$$D_{T,E} = \sqrt{\sum_{x} (I_{th}[x] - I_{exp,n}[x])^2 \,/\, \sum_{x} (I_{th}[x])^2} \quad (27)$$

It is observed that $D_{T,E}$ is between 0.2483 and 0.6522 for the set-up IDs $S1$ to $S8$. It is larger than expected although the peak locations and amplitudes are highly close to each other as shown in Figs. 8 and 9. It is observed that there are small levels of shift at the location of peaks of intensity distributions as shown more clearly in Figs. 9(a) and (b) with peaks not in coincidence leading to larger distance values. The challenges include improving warping operation, increasing resolution of camera and enhancing the quality of the monitor paper.

2) EXPERIMENTAL FUTURE WORKS

A practical solution to improve experimental accuracy during measurement is to replace black paper based monitor screen with CCD or CMOS based sensors and cameras. Two designs are shown in Figs. 13(b) and (c) for utilizing sensor arrays. In Fig. 13(b), the diffraction pattern is focused on the sensor array of a camera based receiver by using a lens [34]. On the other hand, in Fig. 13(c), either a single photodetector or a sensor array is mechanically positioned at different points while covering the complete area of the diffraction pattern. If the number of planes is significantly large for ultra high order modulation capability and a few photons reach the detector, then the best solution becomes to use a large area single photon detector allowing to measure the distribution of the diffracted photons by photon counting. Resolution is improved by increasing the number of pixels and reducing the pixel width on the sensor array.

On the other hand, sensor based measurements shown in Figs. 13(b) and (c) have also some similar challenges with monitor screen based solution. MPD increases the spatial frequency of the signal significantly as shown in simulation studies in Section IV transforming smooth distributions of the intensity of incoming symbols into intensity patterns which are closer to uniformly distributed patterns. Therefore, focusing high spatial frequency distribution to the pixel area of a camera based receiver as shown in Fig. 13(b) without losing the details may be challenging. On the other hand, the design with mobile sensor array shown in Fig. 13(c) requires mechanical movements of the sensor array to cover large area diffraction patterns.

Next, spatial light demodulation set-up is utilized for all-optical symmetric-key cryptography as a promising application in addition to the presented optical communications applications.

VI. FUTURE APPLICATIONS FOR CRYPTOGRAPHY

A novel cryptographic framework based on spatial light demodulation is shown in Fig. 14. Bob encodes input phase-amplitude distribution with respect to spatial light demodulation set-up of Alice composed of diffraction keys $D_j(x, y)$ for $j \in [1, N]$ and integration key $p[k_x, k_y] \in [0, 1]$ denoting the summation of the intensities at a specific sub-set of PDs with the total count in the sub-set being fixed as $N_P / 2$. We assume that detector intensity is normalized for each lth bit $m_l \in [0, 1]$, i.e., $\sum_{k_x} \sum_{k_y} I_{d,m_l}[k_x, k_y] = 1$. We define $d[l]$ denoting detector output as follows:

$$d[l] = \sum_{k_x} \sum_{k_y} p[k_x, k_y] \left(I_{d,m_l}[k_x, k_y] + n[k_x, k_y] \right) \quad (28)$$

Decoding is achieved by using a threshold detector as follows:

$$\widehat{m}_l = \begin{cases} 1 & \text{if } d[l] >= 0.5 \\ 0 & \text{if } d[l] < 0.5 \end{cases} \quad (29)$$

The output includes signal and noise components as $d[l] = d_s[l] + n_d[l]$ where $n_d[l]$ is the integrated noise components of $N_P / 2$ PDs. Since the integrator adds $N_P / 2$ PD outputs, total variance of the noise becomes equal to $\sigma_d^2 \equiv N_P \sigma^2 / 2$.

The details of symmetric-key cryptography is shown in Algorithm VI. In the first step, Alice shares the secret keys $D_j(x, y)$ for $j \in [1, N]$ and $p[k_x, k_y]$ with Bob. Then, in the second step, Bob initializes $M_{1,m_l}(x, y)$ for each $m_l \in [0, 1]$ with a random pattern, e.g., for a phase-only modulation mask choosing each phase value at a single pixel with a uniform distribution. Therefore, intruder Charlie observes randomly distributed patterns without any clue to estimate the bit sequence based on the random initialization in the second step. Bob calculates the noise-free signal at the demodulated output of Alice by using private keys. In the third step, he realizes non-linear optimization for adjusting modulation mask $M_{1,m_l}(x, y)$ initialized with a random pattern to maximize $d_s[l]$ for $m_l = 1$ and to minimize $d_s[l]$ for $m_l = 0$. In Section VI-A, we numerically observe that the optimized patterns are not reliably decoded by Charlie without access to private keys while verifying the efficiency of initialization

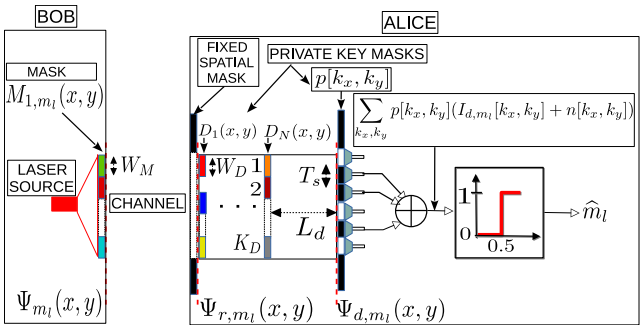

FIGURE 14. All-optical symmetric-key cryptography application of spatial light demodulation where private keys include information about spatial light demodulation masks $D_j(x, y)$ for $j \in [1, N]$ and $p[k_x, k_y] \in [0, 1]$ for $k_x \in [1, N_x]$ and $k_y \in [1, N_y]$ denoted as integrator mask summing the intensities of a specific sub-set of PD array. Demodulator output is fed to a simple threshold detector for decoding. Bob initializes the mask $M_{1,m_l}(x, y)$ with a random pattern for transmitting lth bit value denoted with m_l and optimizes it to increase distance between the demodulator outputs for $m_l = 0$ and 1.

Algorithm 1 Spatial Light demodulation Based Symmetric-Key cryptography Algorith

1) Alice shares secret keys $D_j(x, y)$ for $j \in [1, N]$ and $p[k_x, k_y]$ as the integration mask with Bob.
2) Bob initializes mask $M_{1,m_l}(x, y)$ with a random pattern for transmitting lth bit value denoted with $m_l \in [0, 1]$ with the target of realizing independent patterns for each l.
3) Bob adjusts $M_{1,m_l}(x, y)$ with a non-linear optimization algorithm to minimize and maximize signal demodulator output $d_s[l]$ for $m_l = 0$ and 1, respectively. Then, Bob modulates the incoming initial optical wave pattern with $M_{1,m_l}(x, y)$.
4) Alice decodes by measuring received intensity, calculating $d[l]$ and applying a threshold detector, i.e., $\widehat{m}_l = 0$ if $d[l] < 0.5$ and $\widehat{m}_l = 1$ if $d[l] >= 0.5$.

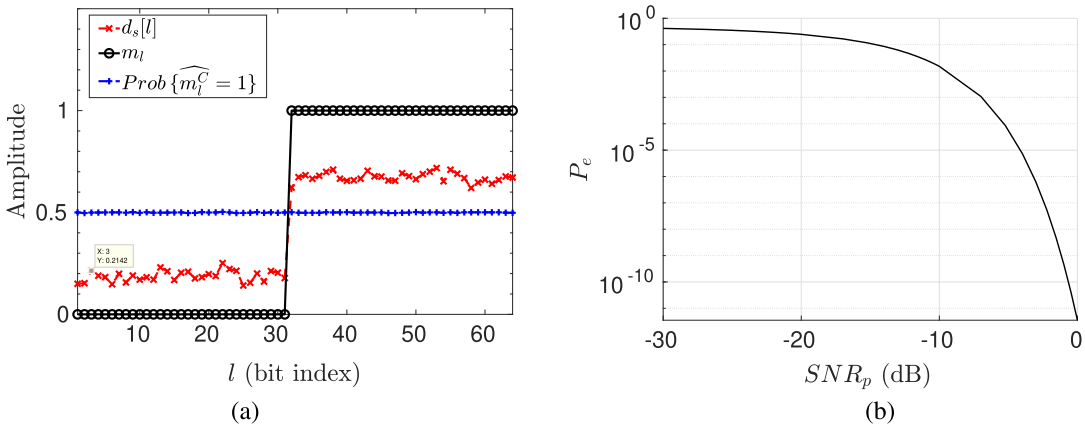

FIGURE 15. All-optical symmetric-key cryptography performance showing the transmission of 64 bit sequence for $l \in [1, 64]$ while m_l values are sorted: (a) the values of demodulator output $d_s[l]$ excluding the effect of noise to observe the possible noise margin, transmitted message bit m_l and probability of decoding as 1 of the intruder Charlie, i.e., $Prob\{\widehat{m_l^C}=1\}$, for varying message bit index l and (b) probability of error P_e in decoding for varying pixel SNR value SNR_p.

with random patterns. In the fourth step, Alice decodes the encoded message m_l.

Assume that, Bob optimizes modulation parameters such that $d_s[l]$ equals to fixed d_{s,m_l} for $m_l \in [0, 1]$. Then, probability of bit error for equally probable symbols is calculated as follows:

$$P_e = \left(p(n_d \geq 0.5 - d_{s,0}) + p(n_d \leq 0.5 - d_{s,1})\right) / 2 \quad (30)$$

where $p(n_d \geq 0.5 - d_{s,0})$ and $p(n_d \leq 0.5 - d_{s,1})$ denote probabilities based on the decoding rule in (29) and n_d is AWGN with variance of $\sigma_d^2 = N_P \sigma^2 / 2$. Assume that intensity is uniformly distributed so that average pixel intensity equals to $1 / N_P$ while pixel SNR becomes $SNR_p = 1 / (N_P^2 \sigma^2)$. Then, P_e is easily calculated as follows by using q-function $Q(x) \equiv (1 / \sqrt{2\pi}) \int_x^\infty e^{-u^2/2} du$ [33]:

$$P_e = \sum_{m_l=0}^{1} Q\left(\sqrt{2 N_p SNR_p |0.5 - d_{s,m_l}|^2}\right) / 2 \quad (31)$$

where it is assumed that the channel is modeled as an AWGN channel with $r = \sqrt{E_b} + n$ while r denotes the received signal, $\sqrt{E_b}$ is the modulation amplitude for a single bit, n is the noise with variance σ_n^2 and threshold level is equal to zero leading to $P_e = Q(\sqrt{E_b / \sigma_n^2})$ for the single bit. In our case $\sqrt{E_b}$ is replaced by $|0.5 - d_{s,0}|$ or $|0.5 - d_{s,1}|$ and σ_n^2 is equal to σ_d^2.

Charlie applies a random mask $p^C[k_x, k_y]$ at the same reception distance with Alice but without any spatial light demodulation. Received intensity with direct detection is denoted as $I^C_{d,m_l}[k_x, k_y]$. Then, he applies threshold detector by obtaining $\widehat{m_l^C}$ to estimate m_l. We define average probability of demodulator signal output to result in one, i.e., $Prob\{\widehat{m_l^C} = 1\}$, for randomly chosen M_r different $p^C[k_x, k_y]$ sequences as follows:

$$\frac{1}{M_r} \sum_{j=1}^{M_r} I_t\left(\sum_{k_x}\sum_{k_y} p_j^C[k_x, k_y]\, I^C_{d,m_l}[k_x, k_y]\right) \quad (32)$$

where $p_j^C[k_x, k_y]$ denotes the random mask at jth trial, $I_t(x)$ is the detector threshold function with output being equal to 0 for $x < 0.5$ and 1 for $x >= 0.5$. It is an open issue to theoretically verify randomness in the pattern for varying symmetric keys.

Assume that each pixel is masked by choosing among G different values depending on the hardware, e.g, 2 for slit based set-ups as in [17]. Then, the worst case complexity of decryption by Charlie requires exponentially growing number of keys $N_C \equiv N_{SLD} N_I$ where $N_{SLD} = G^{K_D^2 N}$ and $N_I = \binom{N_P}{N_P/2}$ are total number of possible spatial light demodulation set-ups and integration keys, respectively.

TABLE 3. Design parameters for numerical simulation of symmetric-key cryptography.

Parameter	Value	Parameter	Value	Parameter	Value
K_M	40	K_D	800	N_x	400
W_M	100 μm	W_D	10 μm	T_s	10 μm

A. NUMERICAL SIMULATION PERFORMANCE OF SYMMETRIC-KEY CRYPTOGRAPHY

Symmetric-key cryptography design in Fig. 14 is simulated for $N = 1$ for simplicity in order to verify capabilities of SPD with further improvement based on MPD with promising results obtained in Sections IV and V. Design parameters for modulation, demodulation and detection showing the widths and total numbers of slits and pixels are shown in Table 3. The phase-only modulator modulates $K_M = 40$ different slits with the width $W_M = 100$ μm by using the phase mask $M_{1,m_l}[k_x]$ for $k_x \in [-19, 20]$. On the other hand, the

demodulator phase only mask slit width is chosen as $W_D = 10$ μm with much larger number of $K_D = 800$ slits. Fixed spatial mask extends between $[-2, 2]$ mm by clipping the received signal before spatial light demodulation. $N_x = 400$ PD pixels along the clipped region have $T_s = 10$ μm. $p[k_x, k_y]$ is chosen as a random sequence composed of zeros and ones. We choose $M_r = 10^5$ for simplicity to calculate $Prob\{\widehat{m_l^C} = 1\}$. The channel and demodulator distances are chosen as $L_c = 500$ mm and $L_d = 150$ mm, respectively.

We simulate transmission of 64 bit message sequence for simplicity with equal probability of 0 and 1 source bits indexed by $l \in [1, 64]$ and then numerically calculate values of $d_s[l] = \sum_{k_x} p[k_x] I_{d,m_l}[k_x]$ without including noise component in the output signal $d[l]$ to observe possible noise margin. The detector intensity is normalized for each message by satisfying $\sum_{k_x} I_{d,m_l}[k_x] = 1$.

The message input sequence m_l is sorted and the corresponding decoded output $d_s[l]$ with optimized masks $M_{1,m_l}[k_x]$ are shown in Fig. 15(a). The optimization of the masks is achieved with non-linear optimization toolbox of MATLAB. It is observed that the optimized modulator mask achieves mean values of $d_{s,0}$ and $d_{s,1}$ being equal to ≈ 0.18 and ≈ 0.67, respectively, based on the obtained values for 64 messages by creating a large noise margin compared with the normalized total intensity of unity. The distance to the threshold is observed to be not equal, i.e., $|0.5 - d_{s,0}| \neq |d_{s,1} - 0.5|$, requiring further optimization in the design in order to realize more balanced key generation as an open issue.

On the other hand, $Prob\{\widehat{m_l^C} = 1\}$ for the random mask of an intruder is shown in Fig. 15(a) with the value of ≈ 0.5 producing a random sequence at the output without access to private keys $D_1(k_x)$ and $p[k_x]$. P_e is calculated for varying SNR_p as shown in Fig. 15(b) with high performance due to the receiver diversity with many pixels.

VII. CONCLUSION

In this article, theoretical modeling, numerical simulation and experimental implementation of MPD based passive spatial light modulation and demodulation designs are presented. Numerical simulations and experimental implementation of demodulation provide proof-of-concept performance improvement compared with direct detection of spatial phase modulated signals, e.g., improving inter-symbol distances by $\approx$2 times at maximum for specific set-up parameters. In addition, MPD based demodulation provides higher performance with increasing number of diffraction layers by improving state-of-the-art interferometric demodulation architectures exploiting only SPD design. We experimentally show the capabilities of randomly distributed slits to demodulate signals with similar intensity but different phase distributions. Besides that, quantum spatial modulation method based on MPD previously defined for improving spatial modulation capability in optical communications is experimentally implemented as a proof-of-concept with simple rectangular slit based diffraction architectures. Furthermore, we apply spatial light demodulation for designing an all-optical free space symmetric-key cryptography system as a novel application of MPD based design architecture. Numerical simulations of symmetric-key cryptography verify security against decoding without access to private keys, respectively. The proposed modulation and demodulation design based on MPD promises important applications in optical communications and cryptography with low-cost, low-complexity and high performance system design. Open issues include designing methods to improve experimental accuracy and verification of complete communication and cryptographic communication systems based on proposed modulation and demodulation mechanisms.

ACKNOWLEDGMENT

Burhan Gulbahar thanks Gorkem Memisoglu for fruitful discussions about experimental procedures and QABACUS Quantum Computer Company Ltd., İzmir, Turkey, for providing support about experimental equipments.

REFERENCES

[1] S. Ahderom, M. Raisi, K. Lo, K. E. Alameh, and R. Mavaddat, "Applications of liquid crystal spatial light modulators in optical communications," in *Proc. 5th IEEE Int. Conf. High Speed Netw. Multimedia Commun.*, Jul. 2002, pp. 239–242.

[2] M. Stalder and M. Schadt, "Linearly polarized light with axial symmetry generated by liquid-crystal polarization converters," *Opt. Lett.*, vol. 21, no. 23, pp. 1948–1950, 1996.

[3] K. J. Mitchell, S. Turtaev, M. J. Padgett, T. Čižmár, and D. B. Phillips, "High-speed spatial control of the intensity, phase and polarisation of vector beams using a digital micro-mirror device," *Opt. Exp.*, vol. 24, no. 25, pp. 29269–29282, Dec. 2016.

[4] L. Zhu and J. Wang, "Arbitrary manipulation of spatial amplitude and phase using phase-only spatial light modulators," *Sci. Rep.*, vol. 4, no. 1, pp. 1–7, May 2015.

[5] J. W. Jian Wang, "Metasurfaces enabling structured light manipulation: Advances and perspectives [invited]," *Chin. Opt. Lett.*, vol. 16, no. 5, 2018, Art. no. 050006.

[6] L. Zhu, J. Liu, Q. Mo, C. Du, and J. Wang, "Encoding/decoding using superpositions of spatial modes for image transfer in km-scale few-mode fiber," *Opt Exp.*, vol. 24, no. 15, pp. 16934–16944, 2016.

[7] L. Wu, S. Cheng, and S. Tao, "Simultaneous shaping of amplitude and phase of light in the entire output plane with a phase-only hologram," *Sci. Rep.*, vol. 5, no. 1, p. 15426, Dec. 2015.

[8] J. Wang, J.-Y. Yang, I. M. Fazal, N. Ahmed, Y. Yan, H. Huang, Y. Ren, Y. Yue, S. Dolinar, M. Tur, and A. E. Willner, "Terabit free-space data transmission employing orbital angular momentum multiplexing," *Nature Photon.*, vol. 6, pp. 488–496, Jun. 2012.

[9] G. Gibson, J. Courtial, M. J. Padgett, M. Vasnetsov, and V. Pas'ko, "Free-space information transfer using light beams carrying orbital angular momentum," *Opt. Exp.*, vol. 12, no. 22, pp. 5448–5456, 2004.

[10] J. Li, M. Zhang, and D. Wang, "Adaptive demodulator using machine learning for orbital angular momentum shift keying," *IEEE Photon. Technol. Lett.*, vol. 29, no. 17, pp. 1455–1458, Sep. 1, 2017.

[11] M. Mirhosseini, M. Malik, Z. Shi, and R. W. Boyd, "Efficient separation of the orbital angular momentum eigenstates of light," *Nature Commun.*, vol. 4, no. 1, p. 2781, Dec. 2013.

[12] Y. Zhao and J. Wang, "High-base vector beam encoding/decoding for visible-light communications," *Opt. Lett.*, vol. 40, no. 21, pp. 4843–4846, Oct. 2015.

[13] Z. Xie, "Spatial phase and polarization retrieval of arbitrary circular symmetry singular light beams using orthogonal polarization separation," *Opt. Exp.*, vol. 27, no. 19, pp. 27282–27294, 2019.

[14] J. Sabino, G. Figueira, and P. André, "Wavefront spatial-phase modulation in visible optical communications," *Microw. Opt. Technol. Lett.*, vol. 59, no. 7, pp. 1538–1541, Jul. 2017.

[15] A. Trichili, K.-H. Park, M. Zghal, B. S. Ooi, and M.-S. Alouini, "Communicating using spatial mode multiplexing: Potentials, challenges, and perspectives," *IEEE Commun. Surveys Tuts.*, vol. 21, no. 4, pp. 3175–3203, 4th Quart., 2019.
[16] J. Li, M. Zhang, and D. Wang, "Adaptive demodulator using machine learning for orbital angular momentum shift keying," *IEEE Photon. Technol. Lett.*, vol. 29, no. 17, pp. 1455–1458, Sep. 1, 2017.
[17] B. Gulbahar and G. Memisoglu, "Quantum spatial modulation of optical channels: Quantum boosting in spectral efficiency," *IEEE Commun. Lett.*, vol. 23, no. 11, pp. 2026–2030, Nov. 2019.
[18] R. Mesleh, H. Elgala, and H. Haas, "Optical spatial modulation," *IEEE/OSA J. Opt. Commun. Netw.*, vol. 3, no. 3, pp. 234–244, Mar. 2011.
[19] J. Fu, C. Hou, W. Xiang, L. Yan, and Y. Hou, "Generalised spatial modulation with multiple active transmit antennas," in *Proc. IEEE GLOBECOM Workshops*, Dec. 2010, pp. 839–844.
[20] C. R. Kumar and R. K. Jeyachitra, "Power efficient generalized spatial modulation MIMO for indoor visible light communications," *IEEE Photon. Technol. Lett.*, vol. 29, no. 11, pp. 921–924, Jun. 1, 2017.
[21] A. Bhowal and R. S. Kshetrimayum, *Advanced Spatial Modulation Systems*. Cham, Switzerland: Springer, 2021.
[22] A. Aytekin and B. Gulbahar, "Experimental analysis of RF based multi-plane-diffraction with over-the-air active cellular signal measurements," in *Proc. 28th Signal Process. Commun. Appl. Conf. (SIU)*, Oct. 2020, pp. 1–5.
[23] X. Lin, Y. Rivenson, N. T. Yardimci, M. Veli, Y. Luo, M. Jarrahi, and A. Ozcan, "All-optical machine learning using diffractive deep neural networks," *Science*, vol. 361, no. 6406, pp. 1004–1008, Sep. 2018.
[24] X. Sui, Q. Wu, J. Liu, Q. Chen, and G. Gu, "A review of optical neural networks," *IEEE Access*, vol. 8, pp. 70773–70783, 2020.
[25] H. Zhou, L. Shi, X. Zhang, and J. Dong, "Dynamic interferometry measurement of orbital angular momentum of light," *Opt. Lett.*, vol. 39, no. 20, pp. 6058–6061, 2014.
[26] H. I. Sztul and R. R. Alfano, "Double-slit interference with Laguerre–Gaussian beams," *Opt. Lett.*, vol. 31, no. 7, pp. 999–1001, Apr. 2006.
[27] C.-S. Guo, L.-L. Lu, and H.-T. Wang, "Characterizing topological charge of optical vortices by using an annular aperture," *Opt. Lett.*, vol. 34, no. 23, pp. 3686–3688, Dec. 2009.
[28] J. Leach, J. Courtial, K. Skeldon, S. M. Barnett, S. Franke-Arnold, and M. J. Padgett, "Interferometric methods to measure orbital and spin, or the total angular momentum of a single photon," *Phys. Rev. Lett.*, vol. 92, no. 1, Jan. 2004, Art. no. 013601.
[29] M. L. F. Abbade, L. D. B. Bobadilla, D. O. de Carvalho, A. A. Ferreira, L. H. Bonani, and I. Aldaya, "All-optical encryption using multi-channel spectral shuffling," *IEEE Photon. Technol. Lett.*, vol. 31, no. 1, pp. 98–101, Jan. 1, 2019.
[30] X. Zhang, W. Li, H. Hu, and N. K. Dutta, "High-speed all-optical encryption and decryption based on two-photon absorption in semiconductor optical amplifiers," *IEEE/OSA J. Opt. Commun. Netw.*, vol. 7, no. 4, pp. 276–285, Apr. 2015.
[31] Y. J. Jung, C. W. Son, S. Lee, S. Gil, H. S. Kim, and N. Park, "Demonstration of 10 Gbps, all-optical encryption and decryption system utilizing SOA XOR logic gates," *Opt. Quantum Electron.*, vol. 40, nos. 5–6, pp. 425–430, Apr. 2008.
[32] H. M. Ozaktas, Z. Zalevsky, and M. A. Kutay, *The Fractional Fourier Transform with Applications in Optics and Signal Processing*. Hoboken, NJ, USA: Wiley, 2001.
[33] J. G. Proakis and M. Salehi, *Digital Communications*, 4th ed. New York, NY, USA: McGraw-Hill, 2001.
[34] W. Rueckner and J. Peidle, "Young's double-slit experiment with single photons and quantum eraser," *Amer. J. Phys.*, vol. 81, no. 12, pp. 951–958, Dec. 2013.

BURHAN GULBAHAR (Senior Member, IEEE) received the B.S. and M.S. degrees in electrical and electronics engineering from Bilkent University, Ankara, Turkey, in 1999 and 2002, respectively, and the Ph.D. degree in electrical and electronics engineering from Koç University, İstanbul, Turkey, in 2012.

From 2015 to 2020, he was an Assistant Professor at the Department of Electrical and Electronics Engineering, Özyeğin University, İstanbul. Since 2020, he has been an Associate Professor with the Department of Electrical and Electronics Engineering, Yaşar University, İzmir, Turkey, and also the Director of the Quantum Computing and Optics Laboratory. His current research interests include quantum computing and communications, quantum optics, neuromorphic computing, nanoscale engineering with 2-D materials, and wireless communications networks. He is a Senior Member of IEEE Communications Society. He is the inventor of 14 granted patents (U.S., EPO, CN) and the author of 35 technical articles/publications. He has received Bell Laboratories Finalist Prize from the Nokia Bell Laboratories, in 2015; the Faculty Information Transfer Excellence Award from Özyeğin University, in 2017; and the Successful Researcher Award from Yaşar University, in 2021.

AHMET EMRECAN OKSUZ was born in Ankara, Turkey, in 1994. He received the B.S. degree in electrical and electronics engineering from Katip Çelebi University, İzmir, Turkey, in 2017, and the M.S. degree from the Department of Nanoscience and Nanoengineering, Dokuz Eylül University, İzmir, in 2021, where he is currently pursuing the Ph.D. degree. He is currently working as a Researcher with the Quantum Computing and Optics Laboratory, Yaşar University. His research interests include quantum optics, fabrication and applications of multifunctional thin films, and synthesis of metal oxide based nanostructures and their applications.